Geophysical Journal International

Geophys. J. Int. (2024) **239,** 258–275
Advance Access publication 2024 July 26
GJI Seismology

https://doi.org/10.1093/gji/ggae260

Influence of upwelling mantle magmas on cratonic crust implied from *Vp*/*Vs* beneath South America platform

Meijian An[1], Mei Feng[1], Marcelo S. Assumpção[2], Marcelo B. Bianchi[2], George S. França,[2] Marcelo P. Rocha[3] and Leda Sánchez Bettucci[4]

[1]*Chinese Academy of Geological Sciences, Beijing,* 100037*, China. E-mail: meijianan@live.com*
[2]*Department of Geophysics, Institute of Astronomy, Geophysics and Atmospheric Sciences, University of São Paulo, São Paulo,* 05508-090*, Brazil*
[3]*Seismological Observatory, Institute of Geosciences, University of Brasília, Brasília,* 70910-000*, Brazil*
[4]*Geophysical Observatory in Uruguay, Faculty of Sciences, University of the Republic, Montevideo,* 11400*, Uruguay*

Accepted 2024 July 19. Received 2024 July 16; in original form 2024 January 30

SUMMARY

The crust of the South American platform recorded imprints of dynamic processes related with the opening of the Central and South Atlantic but has not been well measured. Crustal structure can be retrieved from teleseismic receiver functions using H–κ stacking, but nearly parallel stripes of high stacking values existing in stacking images for seismic stations in sedimentary area cause difficulties in identifying solutions. We show that some seemingly spurious stripes that do not point to any layer solution are helpful in the identification of the solution position. With the aid of the auxiliary stripes, we retrieved thicknesses and *Vp*/*Vs* of sedimentary and crystalline crust for 65 permanent stations of the Brazilian Seismographic Network and six new portable seismic stations in Brazil and Uruguay. The resulted sedimentary thickness and *Vp*/*Vs* exhibit a good correlation with the Phanerozoic sediments in the South American basins. The crust of Paraná–Etendeka Large Igneous Province (LIP) had been expected to be more mafic since it had ever been penetrated by mantle magma in the Cretaceous related to the south Atlantic opening. However, we found very low *Vp*/*Vs* (1.67) in the crystalline crust beneath the LIP, implying a more felsic crust and that no significant mafic intruding/underplating has occurred in the region. The more felsic crust may be formed in a special evolution early than the magmatic event, or during the magmatic event by releasing crustal volatiles. The resulted sedimentary thickness and *Vp*/*Vs* ratios exhibit a good correlation with the Phanerozoic sediments in the South American basins, which implies that Triassic–Jurassic and Cretaceous magmatism did not cause significant metamorphism in sediments formed before the magmatic events.

Key words: South America; Seismic discontinuities; Crustal structure; Large igneous provinces.

1. INTRODUCTION

The influence of ascending magmas from mantle plume on continental lithosphere is often thought to be related to ocean opening and continental break-up (e.g. White & McKenzie 1989), such as enormous-volume mafic rocks extruded in northern Brazil in Triassic–Jurassic and in eastern Brazil in Cretaceous (Fig. 1) which are related to the opening of the Central and South Atlantic (Milani & Filho 2000; Wanderley-Filho *et al.* 2009; Cordani *et al.* 2016). The Cretaceous lava formed one of the largest Large Igneous Provinces (LIP) in the world, the Paraná–Etendeka LIP (Fig. 1; e.g. Sensarma *et al.* 2018). The imprints of the dynamics may be kept in crust since tectonic activities in the areas stopped after the Cretaceous, but have not been well investigated (e.g. Ridley & Richards 2010). Crustal thickness (H) and *Vp*/*Vs* (κ) which reflect crustal evolution and composition can be measured by teleseismic receiver functions (RF, e.g. Langston 1979; Owens *et al.* 1984; Ammon 1991), but with challenge for areas (e.g. the Paraná basin) covered by thick sediments.

Sedimentary cover of low velocity character can delay converted waves from the base of the crust, the Moho (Langston 2011). Besides, multiple reflected waves from sediments (e.g. Sheehan *et al.* 1995; Clitheroe *et al.* 2000; Zhang & Olugboji 2023; Akinremi *et al.* 2024) or ice (e.g. Dahl-Jensen *et al.* 2003; Lawrence *et al.* 2006; Cho 2011; Chaput *et al.* 2014) can contaminate converted waves from the Moho. The two interferences related to sediments make unknown errors in the resulted crustal structure. Joint inversion of receiver functions with surface-wave dispersions (Julià *et al.* 2000;

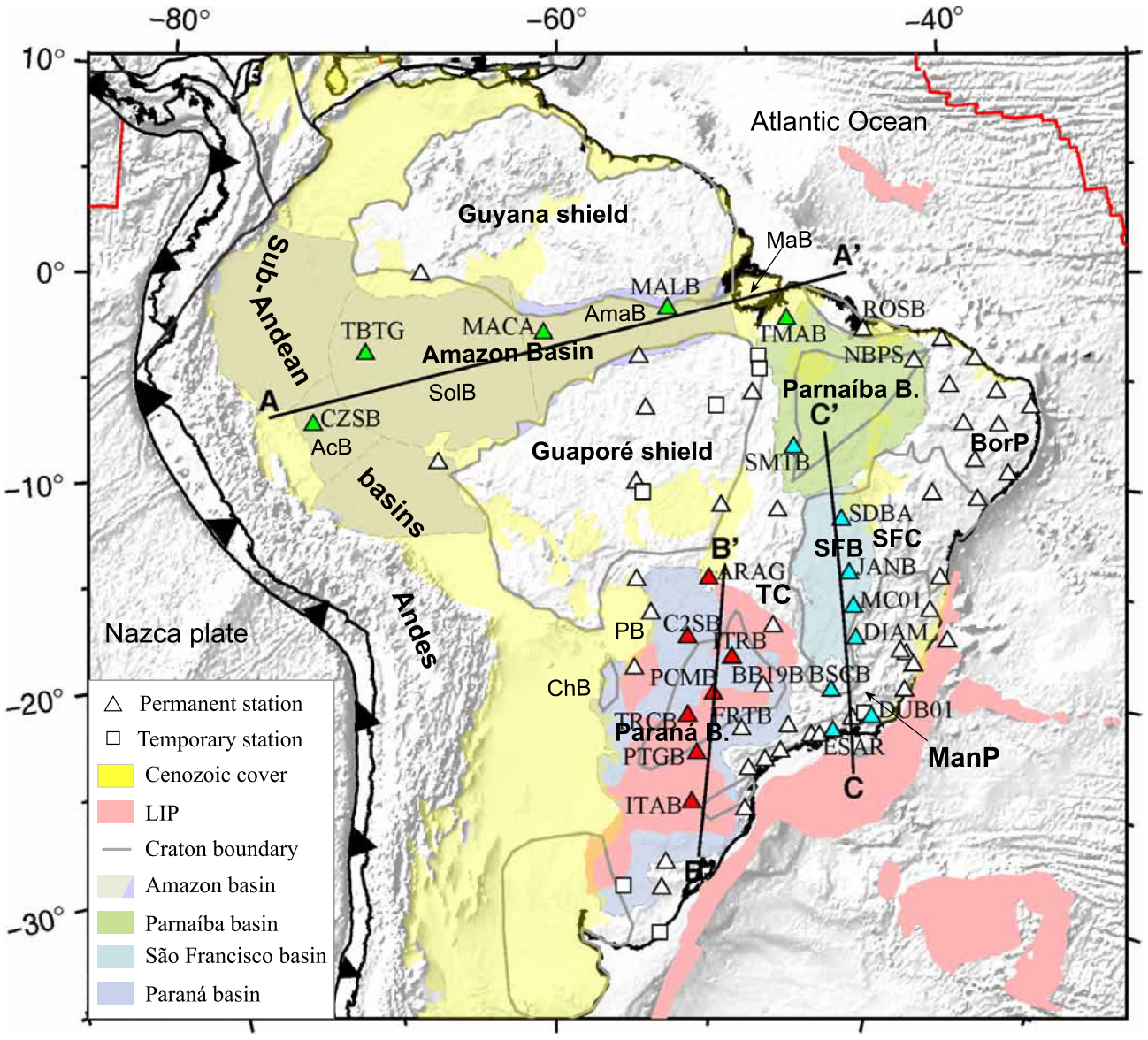

Figure 1. Major basins in South America and seismic stations used in the study. Lines labelled by A–A', B–B' and C–C' are locations for three profiles with seismic stations (Green, red and cyan triangles, respectively) to be discussed in Fig. 9. Geological information is from other literatures, such as Cenozoic covers (Cordani *et al.* 2016), Large Igneous Provinces (LIP, Coffin *et al.* 2013) and basins (Schenk *et al.* 1999). The "Amazon basin" is composed of sub-basins of Acre, Solimões, Amazonas and Marajó basins. AcB = Acre basin, AmaB = Amazonas basin, BorP = Borborema province, ChB = Chaco basin, MaB = Marajó basin, ManP = Mantiqueira province, PB = Pantanal basin, SFB = São Francisco basin, SFC = São Francisco craton, SolB = Solimões basin and TC = Tocantins province.

An & Assumpção 2004b; Feng *et al.* 2017; Cedraz *et al.* 2020) can weaken the two interferences, but the measured surface waves from current sparse stations in some regions of South America (e.g. Amazon basin) are insufficient for a high-quality study. Sedimentary phases can be suppressed to a certain degree by kinds of signal processing (Tao *et al.* 2014a, b; Yu *et al.* 2015; Zhu *et al.* 2018), but the suppressing effects and computational efficiency are very sensitive to parameter settings (Zhang & Olugboji 2021).

H–κ stacking analysis of receiver functions (Zhu & Kanamori 2000) that simultaneously uses the direct *P*-to-*S* converted wave (*Ps*), the 1st multiple (M1 or PpPs) and the 2nd multiple (M2 or PsPs + PpSs) waves from the Moho (Ps_m, $M1_m$ and $M2_m$) may weaken the second interference of phase contamination. Clear sedimentary phases (e.g. An & Assumpção 2004a; Leahy *et al.* 2012) can be used to correct the delayed Moho phases to balance the first interference (Yeck *et al.* 2013; Wei *et al.* 2023). The sequential *H–κ* stacking analysis using the delay-time corrected RFs (Yeck *et al.* 2013) can measure models with sedimentary layer and crystalline crust (Yeck *et al.* 2013; Hajra *et al.* 2019; Zhang & Huang 2019; Wei *et al.* 2020; Gao *et al.* 2022; Akinremi *et al.* 2024) and can be adapted for a multilayer model (Wei *et al.* 2020). However, the *H–κ* stacking image for region with sediments can be so complex that locating/identification of the solution becomes difficult. *A priori* information on crustal structure is helpful, but for sediments, *a priori* information often covers a too wide range (Gercek 2007) to be useful for the *H–κ* analysis.

To solve the problem of solution identification in *H–κ* analysis of RF, we firstly decompose some *H–κ* images of synthetic RFs to

Figure 2. Earthquakes (red circles) used in the study. The blue triangle denotes the centre of all the seismic stations in Fig. 1. For each station, only the earthquakes with epicentral distance between 30° and 95° are used.

understand the complexity of stripes of high stacking values. Two auxiliary stripes of high stacking values around the solution stripe are found to be related to the solution and helpful to identify the solution. With the aid of the auxiliary stripes, we retrieved layered crustal structures beneath stations of the Brazilian Seismographic Network and of portable seismic networks in Brazil and Uruguay by H–κ stacking analysis. The resulted crustal structures are helpful in understanding basin tectonic evolution and influence of mantle-magmas penetration on the crust during the opening of Atlantic.

2. SEDIMENTATION IN SOUTH AMERICAN PLATFORM

After the South American continent was amalgamated from the cratonic blocks during the Brasiliano orogeny (600–530 Ma), its western margins have been affected by oceanic subduction (e.g. Milani & Filho 2000; Martinod *et al.* 2010) (Fig. 1). With successive phases of subsidence and accumulation of sedimentary rocks, five intracontinental basins (Solimões, Amazonas, Parnaíba, Paraná and Chaco-Paraná) inside the South American platform (the central-eastern continent; Fig. 1) were formed since Late Ordovician (∼450 Ma) (Milani & Filho 2000). During the Mesozoic, the basins were successively influenced by mafic magmatic activity related to the opening of the Central and South Atlantic (Milani & Filho 2000), as attested by enormous volumes of Triassic–Jurassic mafic igneous rocks in the Solimões, Amazonas and Parnaíba basins in northern Brazil (Milani & Filho 2000; Wanderley-Filho *et al.* 2009) and of Cretaceous mafic lava in the Parnaíba, Paraná (Milani & Filho 2000; Cordani *et al.* 2016) and São Francisco basins (Reis *et al.* 2017). The subsidence of the above basins stopped after the Cretaceous. In the Cenozoic, weak sedimentation has occurred in the Sub-Andean foreland basins and Amazon drainage basin (yellow shaded areas in Fig. 1).

During the above processes, thick Phanerozoic sedimentary rocks covered the basins. The thickness can be up to 5 km in the Solimões and Amazonas subbasins (Milani & Filho 2000; Wanderley-Filho *et al.* 2009), 2.5 km in the Acre subbasin (Oliveira & Vidotti 2023, 2024), ∼7 km in the Paraná basin (Almeida 1980; Zalán *et al.* 1991; Milani 1992; Milani & Filho 2000) and ∼3.5 km in the Parnaíba basin (Góes & Feijó 1994; Milani & Filho 2000). So, the two interferences of the thick sediments in receiver function analysis should be considered for stations in the basins. Sedimentary rocks have a lower seismic velocity than the crystalline basement, so the crust beneath the basins can be taken as composed of two layers (sedimentary rocks and crystalline crust), while the crust in the other areas of the South American Platform (e.g. Guapore shield, Fig. 1) can be taken as composed of only one crystalline layer. Some of the Cenozoic sediments are unconsolidated with seismic velocity even lower than sedimentary rocks. In this case, the crust beneath the areas can be taken as composed of three layers (unconsolidated sediments, sedimentary rocks and crystalline crust).

3. DATA

We collected seismic waveform data recorded by 65 stations from the Brazilian permanent network (BL, BR, NB and ON, Bianchi *et al.* 2018) from 2015 to 2019 (triangles in Fig. 1) and six new temporary stations in Brazil and Uruguay (rectangles in Fig. 1).

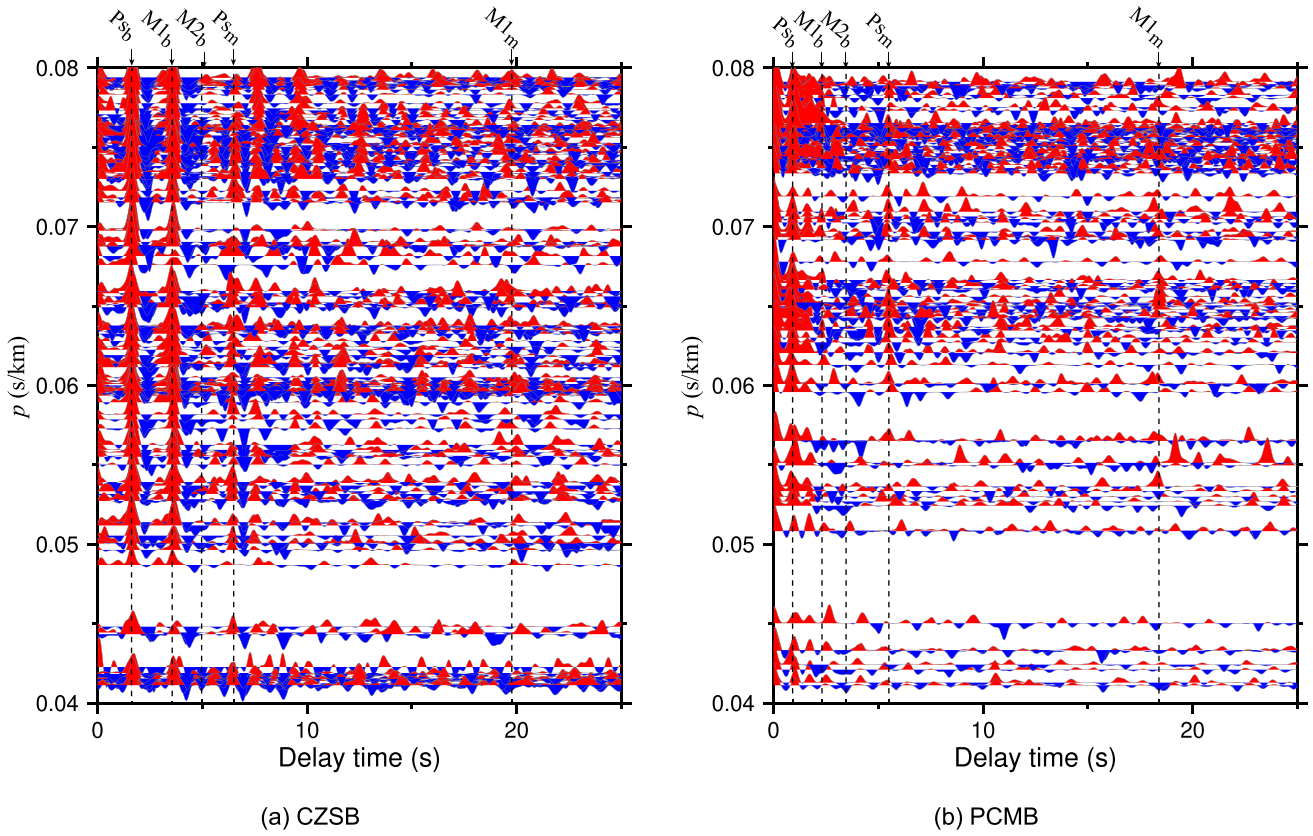

Figure 3. Receiver functions at the (a) CZSB and (b) PCMB stations. A Gaussian width factor of 5 is used in the deconvolution for the receiver functions. The labels Ps_b, $M1_b$ and $M2_b$ are of the primary P-to-S and the 1st and 2nd multiple waves from the base of sediments; Ps_m, and $M1_m$ are of the primary P-to-S and the 1st multiple waves from the Moho.

The temporary stations were deployed under cooperations among institutions from Brazil (University of São Paulo and University of Brasília), China (Chinese Academy of Geological Sciences) and Uruguay (Universidad de la República). We sliced three-component waveforms for teleseismic events (Fig. 2, red circles) with epicentral distance between 30° and 95° and magnitude greater than 5.5. The three component waveforms in the ZNE recording system (vertical, N–S horizontal and E–W horizontal) were rotated to the ZRT (vertical, radial and tangential) coordinate system. Receiver functions are extracted by iterative time-domain deconvolution of radial to vertical component using Gaussian pulses (Ligorría & Ammon 1999) of a width factor of 5 (corresponding to a central frequency of ∼2.4 Hz), by the same processing as in our previous studies (e.g. Feng *et al.* 2014; Feng *et al.* 2017). All receiver functions were visually checked to eliminate those with unclear Ps phase or with long-period oscillations. Receiver functions with potential but confusing Ps phases were initially kept as valid but further checked after the H–κ analysis. Fig. 3 shows the selected receiver functions of the CZSB and PCMB stations after quality control.

4. METHOD

4.1. Definition of variables and symbols

Structure of the ith layer in a m-layer crustal model:

(i) H_i, H_{mi}: Thickness.
(ii) κ_i, κ_{mi}: Vp/Vs.

Phases in receiver function:

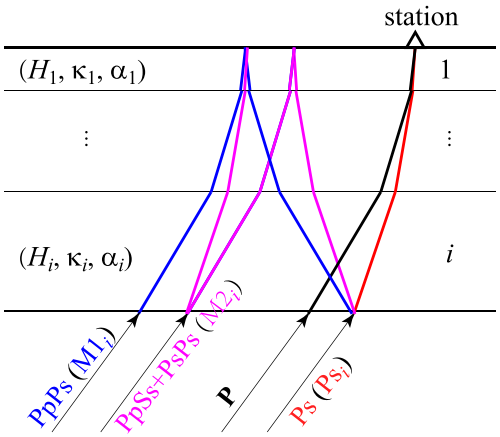

Figure 4. Illustration of paths of converted phases at the ith layer base.

(i) Ps_i, $M1_i$ and $M2_i$: The primary P-to-S converted wave (Ps), 1st multiple wave (PpPs) and 2nd multiple wave (PsPs + PpSs) at the ith layer base.

(ii) tPs_i, $tM1_i$ and $tM2_i$: Observed delay time of the phase Ps_i, $M1_i$ and $M2_i$.

(iii) $t1_i$, $t2_i$ and $t3_i$: Predicted delay time of the phase Ps_i, $M1_i$ and $M2_i$ from a model.

(iv) $A(t)$: Observed amplitude at delay time t.

Stripes of high stacking values in H–κ image:

(i) w_1P: Product of the 1st weight factor w_1 and the amplitude of the *P* phase.

(ii) w_1Ps$_i$ (or w_2Ps$_i$): Product of w_1 (or w_2) and the amplitude of Ps$_i$.

(iii) w_1M1$_i$ (or w_2M1$_i$): Product of w_1 (or w_2) and the amplitude of M1$_i$.

4.2. *H–κ* analysis

For a crust composed of m ($\geq$1) layers, the delay time of a phase converted/reflected at the ith layer base relative to the direct *P* wave (tPs_i, $tM1_i$ or $tM2_i$) is the summation of delays caused by all layers above it (Fig. 4). The delay time in the ith layer can be calculated by subtracting the total delay time by the parts from the 1st to the (i–1)th layers (ΣtPs_j, $\Sigma tM1_j$ or $\Sigma tM2_j$). The ith layer structure (H_i and κ_i) have the following relation with delay times:

$$H_i = \alpha_i \frac{tPs_i - \sum_{j=1}^{i-1} tPs_j}{\sqrt{\kappa_i^2 - \alpha_i^2 p^2} - \sqrt{1-\alpha_i^2 p^2}} = \alpha_i \frac{tM1_i - \sum_{j=1}^{i-1} tM1_j}{\sqrt{\kappa_i^2 - \alpha_i^2 p^2} + \sqrt{1-\alpha_i^2 p^2}}$$
$$= \alpha_i \frac{tM2_i - \sum_{j=1}^{i-1} tM2_j}{2\sqrt{\kappa_i^2 - \alpha_i^2 p^2}}, \quad (1)$$

and

$$\sum_{j=1}^{i-1} tPs_j = \sum_{j=1}^{i-1} tM1_j = \sum_{j=1}^{i-1} tM2_j = 0, \quad \text{if } i = 1, \quad (2)$$

where p is the ray parameter of the incident *P* wave, α_i is the *P*-wave velocity of the ith layer. For any given model, the delay times for the three phases (Ps$_i$, M1$_i$ and M2$_i$) can be predicted using eq. (1). The amplitudes in a radial receiver function at the predicted delay times [$A(t1_i)$, $A(t2_i)$ and $A(t3_i)$] can be stacked using three weighting factors of w_1, w_2 and w_3 (Zhu & Kanamori 2000):

$$s(H_i, \kappa_i) = w_1 A(t1_i) + w_2 A(t2_i) + w_3 A(t3_i). \quad (3)$$

For any given model (H_i and κ_i), when the predicted delay times of the three phases ($t1_i$, $t2_i$ and $t3_i$) coincide with the three observed delay times in receiver functions (tPs_i, $tM1_i$ and $tM2_i$), respectively, the amplitude stack $s(H_i, \kappa_i)$ is expected to be maximum and the model (H_i and κ_i) is considered as the best solution.

Repeatedly using eqs (1) and (3), crustal structure can be sequentially measured layer by layer from top to bottom like layer stripping. When i is 1 for the topmost layer, eq. (1) is the same as eqs (2)–(4) in Zhu & Kanamori (2000), and the measurement of H_1 and κ_1 by eqs (1) and (3) is exactly same as a standard *H–κ* stacking (Zhu & Kanamori 2000). After the topmost layer was measured/stripped, the 2nd ($i = 2$) layer (H_2 and κ_2) can be measured using eqs (1) and (3), which is the same as the sequential *H–κ* analysis (Yeck *et al.* 2013). After stripping the top two layers, we can measure the 3rd layer structure which is the same as the sequential multilayer *H–κ* analysis (Wei *et al.* 2020). Crust of multiple layers can be described by whole crustal thickness (H_a) and average crustal *Vp*/*Vs* (κ_a):

$$H_a = \sum_{i=1}^{m} H_i$$
$$\kappa_a = \sum_{i=1}^{m} \tau_i \kappa_i / \sum_{i=1}^{m} \tau_i, \ \tau_i = \frac{H_i}{\alpha_i}, \quad (4)$$

where τ_i is the time that *P*-wave travels vertically across the i^{th} layer (Fig. 4).

For station with more than one receiver function, the amplitude stacking in eq. (3) should be made for all the RFs. However, RFs from different back azimuths may sample different structure if the structure beneath the station varies azimuthally. To weaken the over-contribution of RFs in dominant azimuths, the inverse of the number of RFs in each 5° of backazimuth bin (n_{az}) is used as a weight ($= n_{az}^{-0.9}$) in the real data *H–κ* stacking analysis, so that RFs in a dominant azimuth bin have a contribution quasi-equal to but slightly higher than the other bins.

High-frequency RFs are thought to be better sensitive to fine layer structures such as the sedimentary layer, while low-frequency RFs are thought to be less affected by high-frequency noise and thus more stable in recovering thick layer structures such as the crystalline crust. So, sedimentary structures determined from high-frequency RFs have been used to correct delay times in low-frequency RFs in determining the crystalline crustal structure (e.g. Yeck *et al.* 2013; Wei *et al.* 2023). However, delay times of phases in practical RFs often slightly vary with frequency, that is phases in high-frequency RFs may be slightly deviated from their counterparts in low-frequency RFs. Correcting delay time by using RFs of different frequencies may introduce extra uncertainties in the results. So, we prefer using high-frequency RFs (with a width factor of 5 for Gassian pulse) both for the sedimentary layer and for the crystalline crust in our *H–κ* analysis. As we can see the example RFs in Fig. 3, the Moho converted waves (Ps$_m$) and the first multiples (M1$_m$) are still well recognizable in the high-frequency RF traces.

4.3. Model space decomposition

Showing together the stacking values of many enumerated models calculated from eq. (3) provides a landscape image of the model space. Ideally, the model at a peak with maximum stacking value in the image is the best solution (Zhu & Kanamori 2000). However, the model space often contains several stripes of high stacking values which may confuse the location of the stacking-extremum (Figs 5c–e), even for the simple case of single-layer model (C1, Sa and Sb, Fig. 5a). For models with two- or multiple-layer crust (C2a and C2b, Fig. 6a), stripes of high stacking values related to different layers may be mutually interfered and identifying the solution in the model space becomes harder (Figs 6b and c). The intensification of landscape around the solution, for example using a cut-off value A_0 in the stack calculation [$s(H_i, \kappa_i) = 0$, if $A(t1_i)$ or $A(t2_i) < A_0$] to rule out some spurious stripes, may be helpful. However, in the following, when decomposing the model space of single-layer models in Fig. 5, we can see that most of the seemingly spurious stripes are very useful to locate solution.

4.3.1. *Objective stripes of solution*

When predicted delay times of the three phases of Ps$_i$, M1$_i$ and M2$_i$ ($m = i = 1$) for a trial model (H_t, κ_t), respectively, coincides with its counterpart in the observed RFs (Fig. 5b), the three amplitude stacking parts of $w_1A(t1_i)$, $w_2A(t2_i)$ and $w_3A(t3_i)$ in eq. (3) will all have large values and form three stripes of w_1Ps$_i$, w_2M1$_i$ and w_3M2$_i$ (or shorten forms w_1Ps, w_2M1 and w_3M2, Fig. 5c) in the *H–κ* stacking image, respectively. The intersection point of the three stripes ('◦' in Fig. 5c) corresponds to the solution (Zhu & Kanamori 2000). So, the three stripes with the best solution are objective stripes to be identified in a *H–κ* stacking image, while the stripes for w_2M1$_i$ and w_3M2$_i$ in practical images may be not clear.

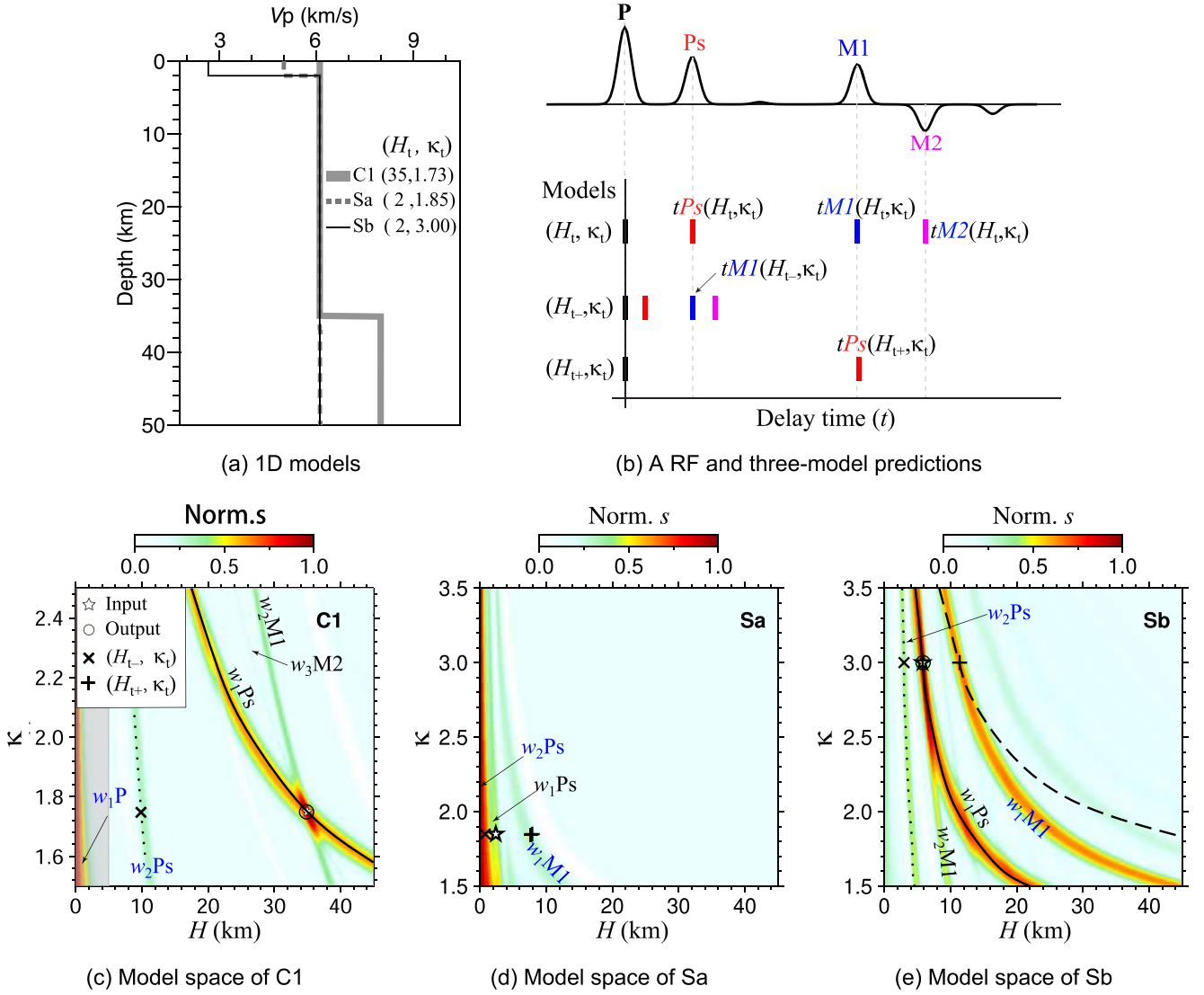

Figure 5. *H*-κ analysis for (a) three synthetic single-layer models. (b) Illustration of delay times for a given trial model (H_t, κ_t) and for its thinner (H_{t-}, κ_t) and thicker (H_{t+}, κ_t) counterpart models. The labels Ps, M1 and M2 are the shorten forms of Ps_1, $M1_1$ and $M2_1$ for single-layer model, respectively. The predicted phase M1 of the model (H_{t-} and κ_t) is coincided with Ps in the synthetic RF for the true model (H_t and κ_t); the predicted Ps of the model (H_{t+} and κ_t) is coincided with the phase M1 in RF. (c–e) *H*-κ model space for three input models. Synthetic receiver functions can be found in the Supporting Information (Figs S1a–c). Solid line in (c, e) marks models in the most prominent objective stripe w_1Ps; dotted line marks the predicted models from all models in w_1Ps by eq. (5); dashed line mark the predicted models from all models in w_1Ps by eq. (6). In (c), as the spurious stripe w_1P has much higher stacking values than the objective stripe w_1Ps, stacking values in the model space of $H \leq 5$ km (grey-shaded area) and those in $H > 5$ km are separately normalized to intensify the objective and auxiliary stripes. For the sake of comparison, *Vp* of model C1 (6.1 km s^{-1}) is used in the stackings for the three models. However, *Vp* of the models Sa and Sb is smaller than 6.1 km s^{-1}, the thicknesses at stack maximum in (d, e) are not same from the input models. In (d, e), the values of w_3M2 are too small and not clear.

4.3.2. *Auxiliary stripes due to mismatching*

If the predicted delay time of a phase (e.g. $t1_i$) does not coincides with its counterpart but with another phase in the observed RFs (e.g. *tP* or $tM1_i$), the weighting factor (e.g. w_1) will mismatch with the unexpected phase's amplitude in eq. (3), and then a spurious stripe with moderately high stacking values may be produced. The stripes of w_1P, w_1M1_i, w_2Ps_i and w_2M2_i (or shorten forms w_1M1, w_2Ps and w_2M2, Figs 5c–e) are produced due to such kind of mismatching.

If the thickness H_1 of a trial model is close to 0, the Ps arrives close to the direct *P* wave. Then the part of $w_1A(tPs)$ in eq. (3) is roughly equal to $w_1A(t\mathrm{P})$. As the direct *P* wave often has the highest amplitude in RF (Fig. 5b), all the trial models with small H_1 will produce a stripe w_1P with the highest stacking values around $H = 0$ in the *H*–κ stacking image (e.g. Fig. 5c).

If the predicted delay time of the phase $M1_i$ ($t2_i$) for a trial model [e.g. (H_{t-}, κ_t)] coincides with the phase Ps_i in the observed RF (Fig. 5b), the part $w_2A(t2_i)$ in eq. (3) actually becomes $w_2A(tPs_i)$. All the trial models due to mismatching of w_2 with the phase Ps_i will form a spurious stripe w_2Ps_i (w_2Ps, Figs 5c–e) which is on the left of the objective stripe w_1Ps_i (w_1Ps, Figs 5c–e). Since w_2 is often set as slightly smaller than w_1, the values of w_2Ps_i are slightly smaller than w_1Ps_i. Similarly, if the predicted delay time of the phase Ps_i ($t1_i$) from a trial model [e.g. (H_{t+}, κ_t)] coincides with $tM1_i$ in observed RF (*tM1*, Fig. 5b), the part $w_1A(t1_i)$ in eq. (3) is actually equal to

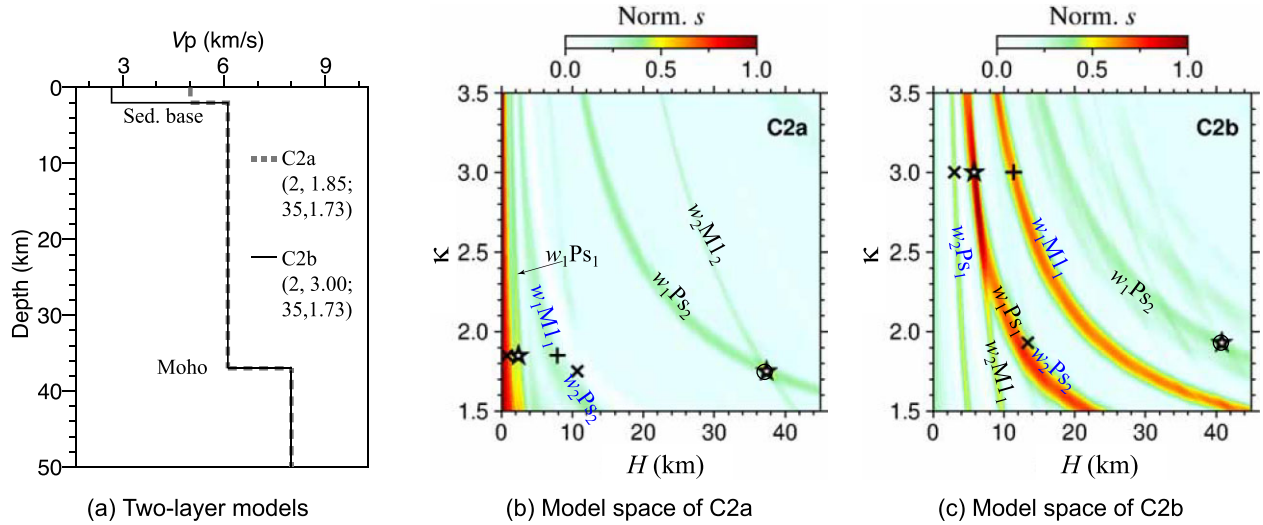

Figure 6. (b,c) H–κ model space for (a) two synthetic models. Synthetic receiver functions can be found in the Supporting Information (Figs S1d and e). *Vp* of 6.1 km s^{-1} is used in the stackings. The symbols are the same as in Figs 5(c)–(e). The circle in (b, c) marks the location of the solution related to Ps_m like in a general H–κ analysis; the star close to the circle marks the model (H_a, κ_a) with the total crustal thickness and average *Vp*/*Vs* (eq. 4).

$w_1A(tM1_i)$. Then another spurious stripe w_1M1_i (w_1M1, Figs 5c–e) due to mismatching of w_1 with the phase $M1_i$ will be formed on the right of the objective stripe w_1Ps_i.

4.3.3. *Locating solution with the aid of auxiliary stripes*

When $m > 1$ (Fig. 6a), the objective stripes and the spurious stripes from different layers may be overlapped/intersected in the model space, so the solution for each layer are difficult to be identified (Figs 6b and c). The above model-space decomposition explicates that the spurious stripes (e.g. w_2Ps and w_1M1, Fig. 5c) are actually originated from observed phases, and then have predictable positional relation to the solution and objective stripes (e.g. w_1Ps, Fig. 5c). The predictable positional relations between the spurious stripes and the objective stripes can be used to verify/identify the objective stripe and solution. Then, the spurious stripes become auxiliary.

For any model (H_i, κ_i) on the objective stripe w_1Ps_i (w_1Ps, solid line in Figs 5c and e), a counterpart thinner model with the same κ_i (H_{i-}, κ_i) can be obtained by replacing $tM1_i$ in the part with $tM1_i$ of eq. (1) by tPs_i:

$$H_{i-} = \alpha_i \frac{tPs_i - \sum_{j=1}^{i-1} tPs_j}{\sqrt{\kappa_i^2 - \alpha_i^2 p^2} + \sqrt{1 - \alpha_i^2 p^2}}. \quad (5)$$

We can find that the set of thinner models predicted by eq. (5) are actually locating on the left auxiliary stripe w_2Ps (dotted line in Figs 5c and e). In another word, if the predicted model (H_{i-}, κ_i) for the model (H_i, κ_i) does not appear on any stripe of high stacking values, the model (H_i, κ_i) should not be the solution.

Similarly, for any model (H_i, κ_i) on the objective stripe w_1Ps_i, a counterpart thicker model with the same κ_i (H_{i+}, κ_i) can be obtained if tPs_i is replaced by $tM1_i$ in the left part (with tPs_i) of eq. (1):

$$H_{i+} = \alpha_i \frac{tM1_i - \sum_{j=1}^{i-1} tM1_j}{\sqrt{\kappa_i^2 - \alpha_i^2 p^2} - \sqrt{1 - \alpha_i^2 p^2}}. \quad (6)$$

We can find that the set of thicker models predicted from all the models on w_1Ps_i by eq. (6) (dashed line in Fig. 5e) are not locating on but intersecting with the right auxiliary stripe w_1M1_i (w_1M1, Fig. 5e) and only the intersecting point (marked as '+' in Fig. 5e) has the same κ_i as the solution. In another word, if the predicted model (H_{i+}, κ_i) for the given model (H_i, κ_i) does not appear on any stripe, the model (H_i, κ_i) is not the solution.

In summary, if a trial model (H_t, κ_t) happens to be the best solution, it must locate on one of the most prominent objective stripes (w_1Ps_i). Its thinner (H_{t-}, κ_t) and thicker (H_{t+}, κ_t) counterpart models estimated by eqs (5) and (6) should respectively appear on two auxiliary stripes on the left and right ('×' on the dotted line and '+' on the dashed line). Otherwise, the trial model should not be the best solution. So, auxiliary stripes together with predicted thinner and thicker counterpart models are helpful to identify the objective stripe and locate the solution, especially for multiple-layer cases (C2a or C2b in Fig. 6, or C3 in Fig. S2 in the Supporting Information).

4.4. Uncertainties

If a delay-time uncertainty of 1/8 period of the converted *S* wave (at frequencies of ~2 Hz) in a velocity of ~2 km s^{-1} for sedimentary rocks is assumed, the layer thickness may contain an uncertainty of ~0.1 km, or say, we cannot resolve layer thickness smaller than 0.1 km.

The amplitude stacking for the ith layer (eq. 1) uses the delay times of the phases of the overlying layers (1st to (i−1)th). If the phases of the overlying layers are reliable and exact, uncertainties in the resulted H and κ of the overlying layers will not influence the stacking for the ith layer. That is, the uncertainties of H and κ for the sedimentary layer will not influence the resulted structure of the crystalline crust. So, uncertainties of each layer are estimated independently, as below.

4.4.1. *Stacking process*

A bootstrap analysis (Efron & Tibshirani 1991) is a way to estimate uncertainties in RF stacking (Crotwell & Owens 2005), but is

inefficient for stations with a large number of receiver functions or inapplicable for stations with a few receiver functions. Uncertainty estimation directly using contours or partial derivatives is efficient but may fail for complex H–κ images (Zhu & Kanamori 2000; Crotwell & Owens 2005; Eaton *et al.* 2006; Ogden *et al.* 2019), especially for cases with sedimentary layers. Here, the landscape around the solution (the peak) in H_i–κ_i stack image is approximated/fitted by a Gaussian function, and the half widths of the Gaussian approximation in the horizontal direction and in the vertical direction are taken as uncertainties for H and for κ [$\sigma_{\mathrm{H},i}(s)$, $\sigma_{\mathrm{k},i}(s)$], respectively. Gaussian approximation around the peak is always valid no matter how complex the landscape is. A grid-search for the best-fitted Gaussian function is more efficient than bootstrap calculations.

4.4.2. *Vp*

Error in *a priori Vp* for the *i*th layer ($\Delta\alpha_i$) rarely influences the resulted κ_i (Zhu & Kanamori 2000), but can deviate the resulted H_i (eq. 1). The thickness obtained by eq. (1) using *Vp* of $c\alpha_i$ [$H_i(c\alpha_i)$] has a relation with that using α_i [$H_i(\alpha_i)$]:

$$H_i(c\alpha_i) = cH_i(\alpha_i)\frac{\sqrt{\kappa_i^2 - \alpha_i^2 p^2} - \sqrt{1 - \alpha_i^2 p^2}}{\sqrt{\kappa_i^2 - c^2\alpha_i^2 p^2} - \sqrt{1 - c^2\alpha_i^2 p^2}} \approx cH_i(\alpha_i), \quad (7)$$

where $\alpha_i{}^2p^2$ ($<\sim$0.15) is always much smaller than 1 and κ^2 ($>\sim$2.2). So, H_i is quasi proportional to *a priori Vp*.

Tests in a standard H-κ analysis for a model with a crust of 35 km (Feng *et al.* 2017) showed that an error of 0.5 km s^{-1} ($\sim$7.7 per cent) in crustal *Vp* (6.5 km s^{-1}) may cause a deviation of $\sim$3–5 km ($\sim$10 per cent) in crust thickness. However, the resulted H_i is proportional to delay times (eq. 1), while the delay time of Ps phase converted at the base of the sediments ($\mathrm{Ps_b}$) is much smaller than that of the Moho ($\mathrm{Ps_m}$). Tests here for a model with 2 km sediments and 35 km crystalline crust show that $\Delta\alpha_i$ of 0.5 km s^{-1} (25 per cent for sediments or $\sim$7.7 per cent for crust) can cause 0.5 km (25 per cent) of deviation for sediments or 3 km (8.7 per cent) for crystalline crust. Here, thickness uncertainties [$\sigma_{\mathrm{H},i}(\Delta\alpha_i)$] of 0.5 km for sediment and 3 km for crystalline crust are assumed.

4.4.3. *Total uncertainties*

The total uncertainty of κ_i is directly given by the half width of Gaussian approximation [$\sigma_{\mathrm{k},i}(s)$] caused by the stacking process since κ_i is not strongly affected by *a priori Vp*. The total uncertainty of H_i is contributed by both the stacking process and the *a priori Vp* and given by:

$$\sigma_{\mathrm{H},i}(\Delta\alpha_i, s) = \sqrt{[\sigma_{\mathrm{H},i}(\Delta\alpha_i)]^2 + [\sigma_{\mathrm{H},i}(s)]^2}. \quad (8)$$

The root sum of squares of $\sigma_{\mathrm{H},i}(\Delta\alpha_i,s)$ of all layers is taken as the uncertainty of the whole crust thickness (σ_{Ha}). The resulted sedimentary *Vp*/*Vs* (κ) can be strongly influenced by data noise and signal frequencies and may have a large uncertainty. *Vp*/*Vs* of sediments is controlled by many factors, such as composition, consolidation, crack, porosity and water saturation (e.g. Tatham 1982; Dunn & Ledbetter 1995; Mavko *et al.* 1998) and then can vary in a large range. So, it is difficult to judge whether the large uncertainties of sediments are a reflection of real structures or affected by data noise. However, *Vp*/*Vs* of crystalline crust varies in a small range (Christensen 1996) and has a small uncertainty. We thus did not estimate the uncertainty for the whole crust.

5. RESULTS

For each station, we firstly evaluated the possible number of layers in the crust by identifying phases in receiver functions and objective stripes in a full H–κ model space (left-hand column of Fig. 7) with an assumption of $m = 1$ and a fixed *Vp* of 6.4 km s^{-1}. Most of the stations have a layer of consolidated sedimentary rocks above crystalline crust which is suitable using a two-layer model ($m = 2$) to process the H–κ analysis. The grid searching ranges for H for sedimentary layer and crystalline crust are set as 0–7 km and 25–55 km. *Vp*/*Vs* of crystalline crust varies in a small range, such as 1.70–1.84 for common plutonic igneous rocks (Christensen 1996), but that of sediment varies in a very large range (Tatham 1982; Bauer & Conley 1987; Dunn & Ledbetter 1995; Bhasin & Høeg 1998; Mavko *et al.* 1998; Min & Jing 2003; Gercek 2007). So, the searching ranges for κ for sedimentary layer and crystalline crust are set as 1.5–2.5 and 1.5–1.9. The basins with Cenozoic cover (Fig. 1) may have one more layer of unconsolidated sediments, then the stations in the area are processed using a three-layer model ($m = 3$). The searching ranges of H and κ for the unconsolidated sediments are set as 0–5 km and 1.7–3.0, respectively. The above searching ranges can be adjusted according to results in previous studies (Assumpção *et al.* 2013; Rivadeneyra-Vera *et al.* 2019; Shirzad *et al.* 2019; Cedraz *et al.* 2020; Nascimento *et al.* 2021; Bernardes *et al.* 2023) and practical solution location. The steps of grid searching for H and κ are all set as 0.1 km and 0.001, respectively. Considering that the multiple converted waves from sedimentary layers are more prominent than from the crystalline crust, the weighting factors (w_1, w_2, w_3) for sediments are set as (0.5, 0.3, −0.2) and for the crystalline crust are set as (0.6, 0.3, −0.1).

A good *Vp* is needed in stacking since the resulted layer thickness (H_i) varies with the given *Vp* (eqs 1 or 7). Unconsolidated sediments have low *Vp*, for example generally 2.0–3.0 km s^{-1} in continent (Mooney *et al.* 1998). Here, a *Vp* of 2.5 km s^{-1} is used in the stacking. The Paraná basin is covered by wide-spread flood basalt (Almeida 1980; Zalán *et al.* 1991; Milani 1992; Milani & Filho 2000), a *Vp* of 5.0 km s^{-1} is used for the consolidated sedimentary layer beneath stations in the basin (An & Assumpção 2006, Fig. 1) and 4.0 km s^{-1} for sedimentary layer out of the Paraná basin. *Vp* of the crystalline crust for the stations in/around the Paraná basin is set as 6.3 km s^{-1} by considering regional tomographic results (Shirzad *et al.* 2019; Cedraz *et al.* 2020) and 6.4 km s^{-1} is set for the other stations, same as in Rivadeneyra-Vera *et al.* (2019).

Typical stacking images for real data are shown in Fig. 7. The measured results for all the seismic stations are shown in Fig. 8 and listed in Table S1. H_s and κ_s are used to denote the total thickness and average *Vp*/*Vs* of sedimentary layers; and H_c and κ_c to the thickness and *Vp*/*Vs* of the crystalline crust. The resulted thickness of a layer (H_i) is obviously related to the given *Vp* (α_i) (eq. 7), but the *P*-wave traveltime vertically through the layer (τ_i, eq. 4) does not (eq. 1). So, we also provided the traveltimes for sediments and crystalline crust in Table S1 (τ_s and τ_c). Receiver functions of several stations with problems are shown in Figs S3–S5 and described in section 'S3 Problems for some stations' in the supplementary file. Lateral variation of the basement and the Moho across the Amazon, Paraná and São Francisco basins (Fig. 1) is shown as profile A–A', B–B' and C–C' in Fig. 9, respectively.

5.1. Typical model space

Ideally, the best solution in a H–κ model space is located at the intersection point of three objective stripes (w_1Ps, w_2M1 and w_3M2,

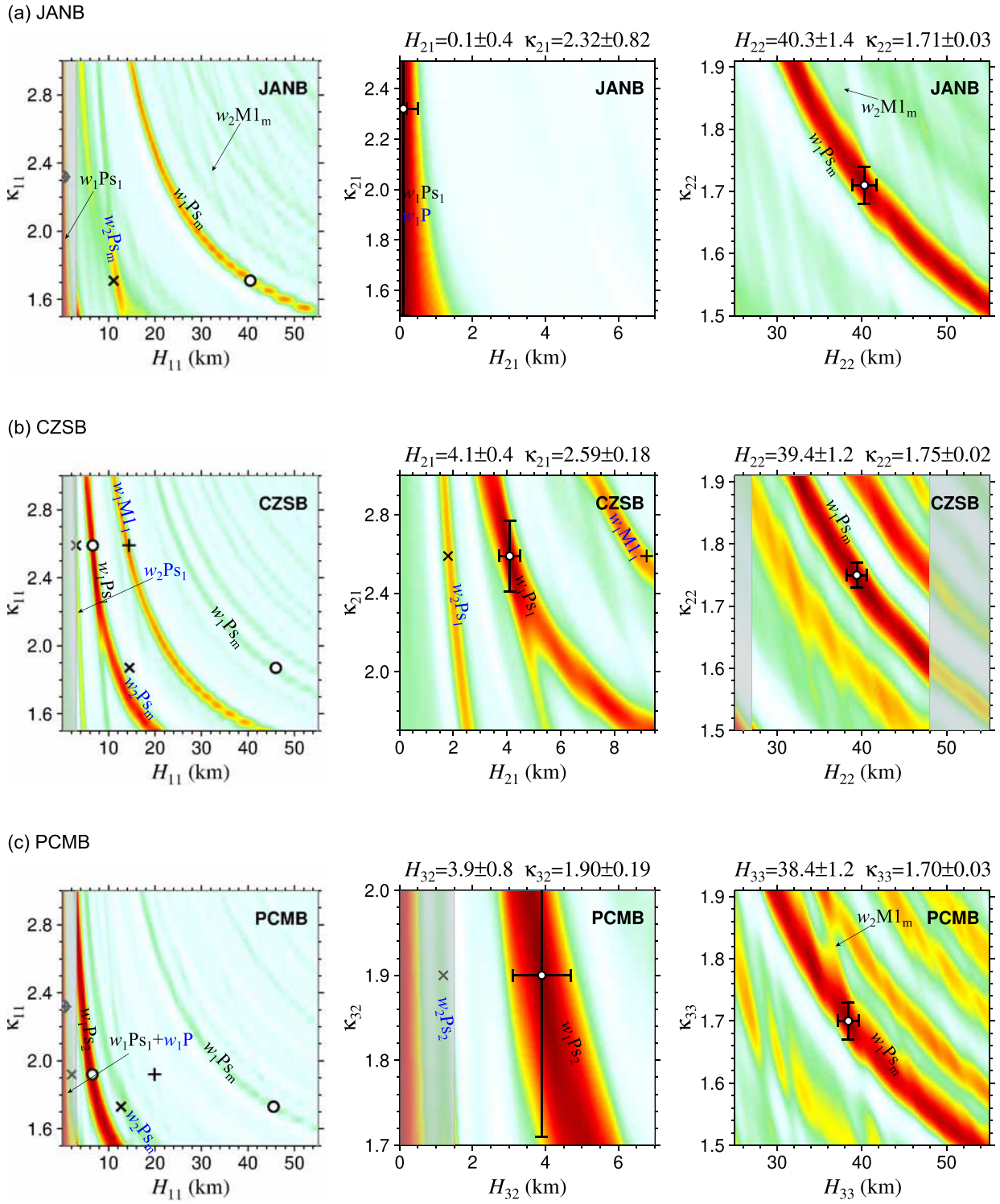

Figure 7. Full model space (left-hand panels) and model space for sediment (middle) and for crystalline crust (right-hand panels) at the JANB, CZSB and PCMB stations. Colour scale is the same as in Fig. 6. Receiver functions of the CZSB and PCMB are shown in Fig. 3. A three-layer crust is assumed for the PCMB ($m = 3$), but the retrieved topmost layer with unconsolidated sediment is too thin ($H_{31} = 0.1$ km) like H_{21} of JANB in (a), so the H_{31}-κ_{31} model space for PCMB is not shown here. In the H-κ model space for a layer (middle and right), the best solution (labelled above the top of the plot) is marked as white circle with error bars. In the full model space (left column), the solutions are (H_s, κ_s) and (H_a, κ_a) in Table S1. '×' and '+' mark the predicted models by eqs (5) and (6) which are respectively locating on the left and right auxiliary stripes of the solution (w_2Ps$_i$, w_1M1$_i$).

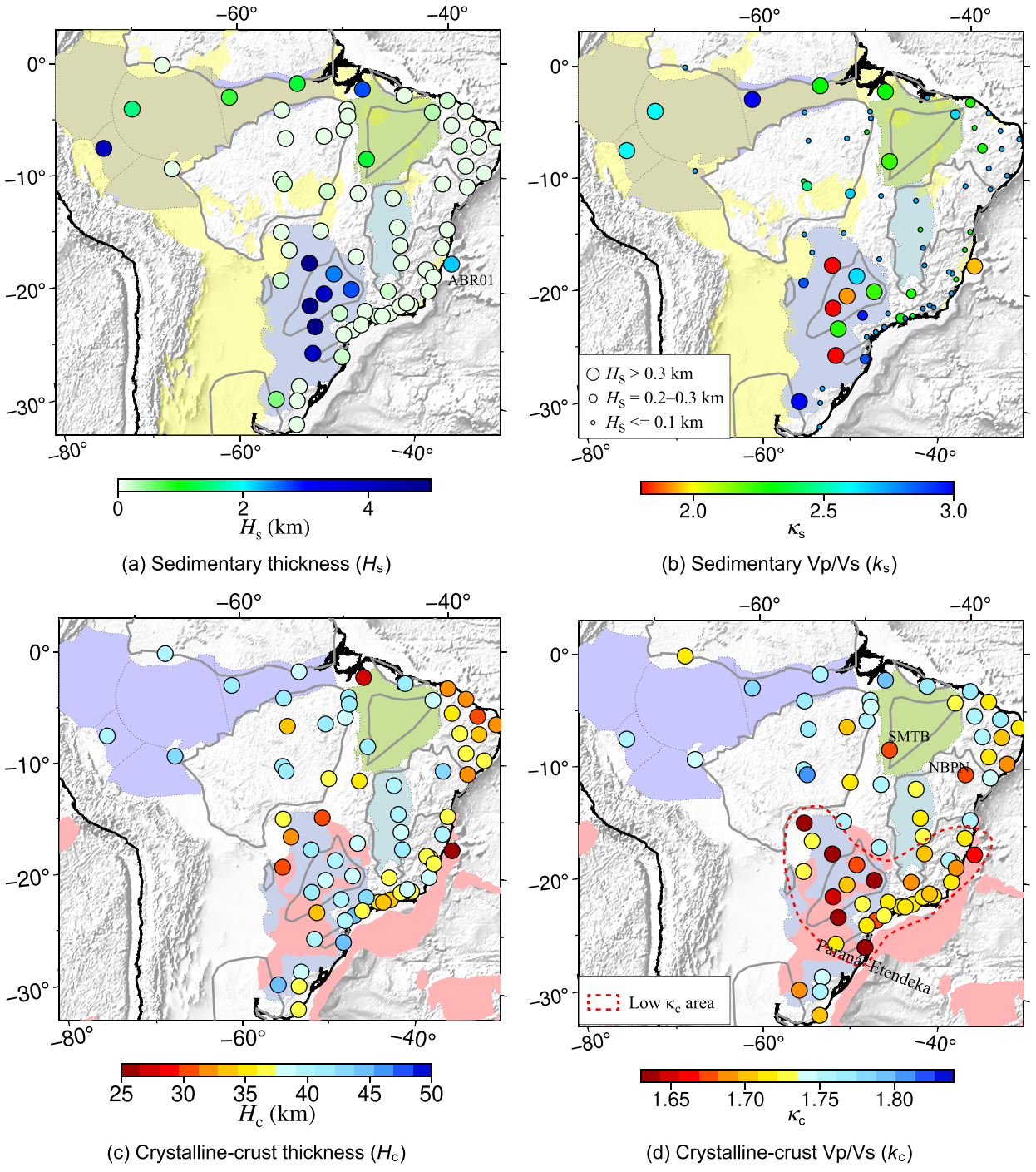

Figure 8. Results of thicknesses (a, c) and *Vp*/*Vs* (b, d). Filled polygons (geology and basin) are the same as in Fig. 1.

Figs 5c–e). However, the first and second multiple phases (M1 and M2) for practical data (Fig. 3) are often not as prominent as synthetic data because of noise contamination and complex structures. So, the stripe w_2M1 of the first multiple is not always recognizable, let alone the weaker stripe w_3M2 of the second multiple. In this case, checking if the predicted thinner and thicker models for a given model by eqs (5) and (6) ('×' and '+', Fig. 7), respectively, are on the left (w_2Ps) and right (w_1M1) auxiliary stripes is helpful to verify the solution location ('o', Fig. 7).

The *H*–*κ* model space for most stations looks like the JANB station in the São Francisco basin (Fig. 7a) with two obvious high-value stripes, similar to the synthetic model C2a (Fig. 6b). The leftmost one around 0 km corresponds to w_1P or a mixture of w_1P and w_1Ps$_1$, which indicates a very small or ignorable

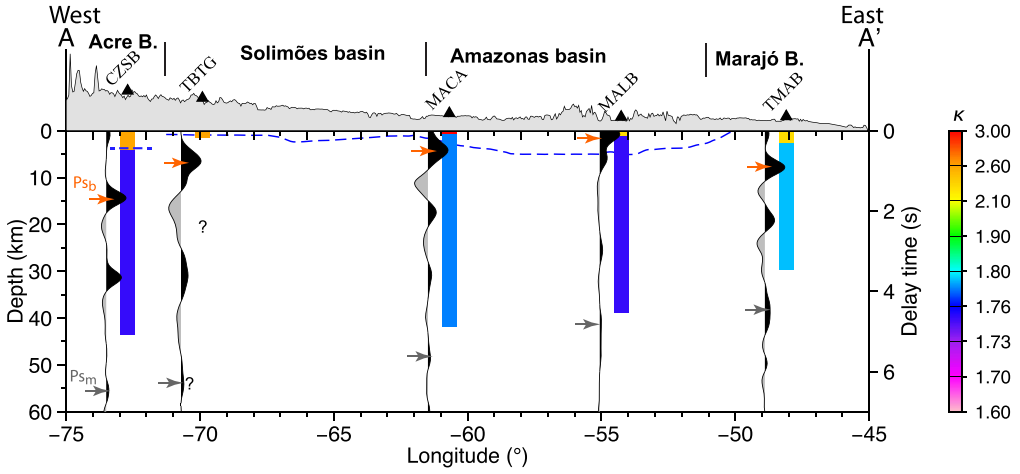

(a) Amazon Basin

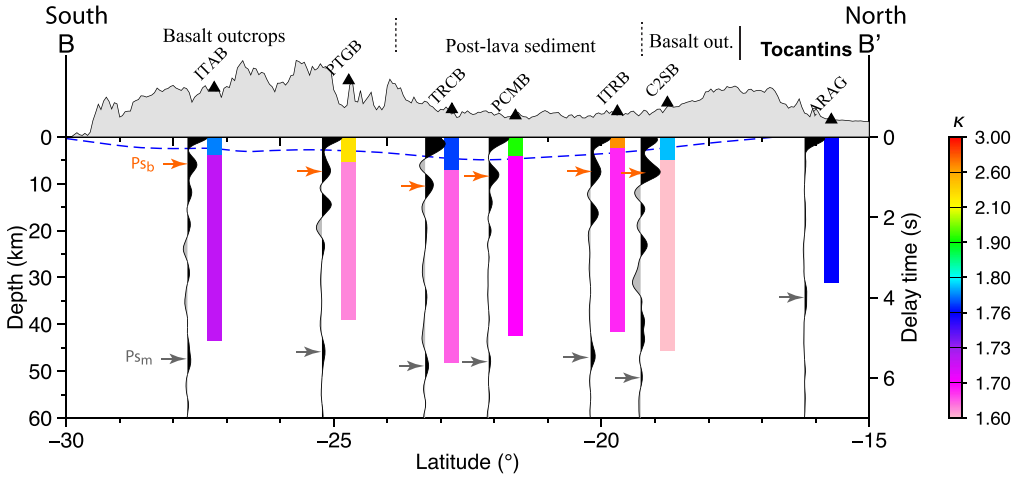

(b) Paraná Basin

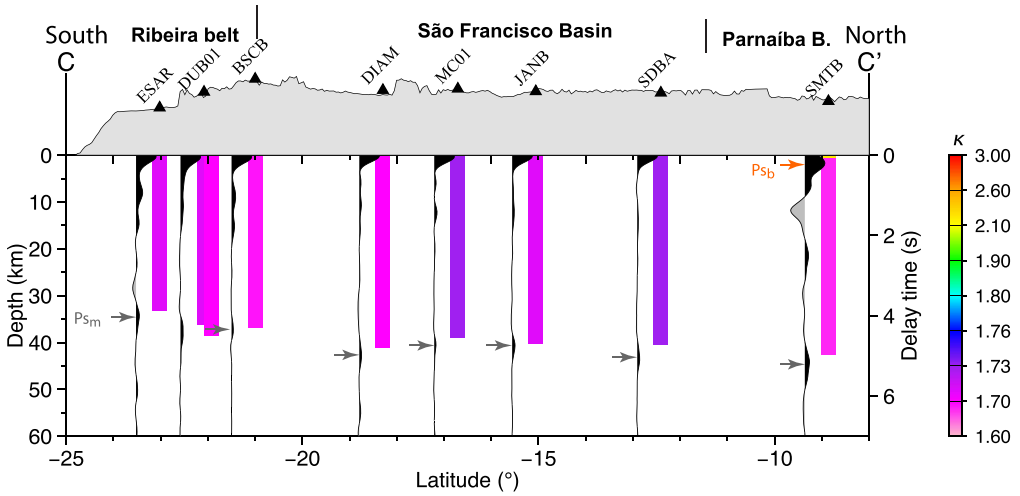

(c) São Francisco Basin

Figure 9. Structure profiles across the Amazon (a), Paraná (b) and São Francisco basins (c). The left- and right-hand vertical axes are, respectively, scale to depth and delay time. The depths of the coloured columns are derived from H_s and H_c; column colours are scaled to κ_s and κ_c; Wiggled waves are RF stack for each station. Black and grey wavelets indicate positive and negative stacks, respectively. Red and grey arrows point to the primary converted waves from the base of sediment (Ps_b) and the Moho (Ps_m), respectively. Blue dashes mark the sedimentary base for the Amazon (Wanderley-Filho *et al.* 2009), Acre (Oliveira & Vidotti 2023, 2024) and Paraná basins (An & Assumpção 2004a).

sedimentary layer. As expected, the resulted thickness for the topmost layer (H_{21} = 0.1 km, middle plot of Fig. 7a) is equal to the searching step and then insignificant, or say, the crust beneath the JANB station can be taken as one crystalline layer. The right high-value stripe corresponds to the objective tripe of $w_1\mathrm{Ps_m}$ for the Moho, which can be confirmed by the consistency between the predicted thinner model (×) with the left auxiliary stripe $w_2\mathrm{Ps}$ (Fig. 7a).

The H-κ model space for some stations looks like the CZSB station in the Amazon basin (Fig. 7b) that dominates by several nearly parallel high-value stripes, similar to the synthetic C2b (Fig. 6c) that contains one thick sedimentary layer of high κ and one crystalline crust. The objective stripe for the sedimentary layer ($w_1\mathrm{Ps_1}$) and its left auxiliary stripe ($w_2\mathrm{Ps_1}$) can be well recognized to locate the sedimentary solution (H_{21} = 4.1 km, κ_{21} = 2.59), which is with a high κ, as expected (middle plot in Fig. 7b). The objective stripe for the Moho ($w_1\mathrm{Ps_m}$) is well separated from the other stripes. Although the stripe for the multiple $w_2\mathrm{M1}_m$ seems invisible in the model space (right plot in Fig. 7b), the multiple phase $\mathrm{M1_m}$ is well recognizable in the RFs (Fig. 3a), which will definitely take effects in the stacking and provide a reasonable Moho solution (H_{22} = 39.4 km, κ_{22} = 1.75) which is consistent with the neighbouring stations.

The H–κ model space for some other stations looks like the PCMB station in the Paraná basin (Fig. 7b) that dominates by two stripes of very high stacking values for small thicknesses, similar to the three-layer synthetic case in Fig. S2 that contains one unconsolidated sedimentary layer, one consolidated sedimentary layer and one crystalline crust. The thickness of unconsolidated (porous or cracked) sediments (Fig. 1) varies laterally in South America and can be up to hundred metres (Milani & Filho 2000; Wanderley-Filho *et al.* 2009), for example >260 m in area close to the MALB station (Serviço Geológico do Brasil, https://siagasweb.sgb.gov.br). Full model space analyses (e.g. left-hand plot of Fig. 7c) show that 9 stations (ABR01, BB19B, C2SB, ITRB, MALB, PCMB, PTGB, SMTB and TRCB) may have unconsolidated sediment layer. However, the assumed unconsolidated sedimentary layer seems too thin. For the case of PCMB, $w_1\mathrm{Ps_1}$ is around 0 km (Fig. 7c), so the crust can be taken as composed of one consolidated sedimentary layer and a crystalline crust, similar to the two-layer case for the CZSB station in Fig. 7b. The model-space for the PCMB station contains nearly parallel stripes, like the CZSB case. The stripes can cause confusion and difficulty in locating the solution. In this case, the consistency between the auxiliary stripes ($w_2\mathrm{Ps}$, $w_1\mathrm{M1}$) and the predicted thinner and thicker models (×, +) for sediment (middle plot) and for the Moho (left plot) are helpful to confirm the final solutions. However, crowded near-parallel stripes may imply that the receiver functions have unexpected or unknown peaks/troughs which can interfere the interested phases and introduce errors in the results.

5.2. Sediments

Both the H_s and κ_s exhibit zoning features that are generally related to the tectonic environment. Thick sediments are found beneath the Paraná basin (mean H_s = 3.9 km), Amazon basin (1.5 km), Parnaíba basin (1.1 km) and beneath the station ABR01 at the continental margin, while thin or ignorable sediments are observed beneath the other areas, as expected (Fig. 8a, Table S1). Very large κ_s is found beneath the Amazon basin (mean κ_s = 2.62) and the Parnaíba basin (2.48), with the maximum beneath the MACA station (3.0). The Paraná basin has strongly laterally varied κ_s with larger values on the edge (>2.17) and smaller values in the centre (∼1.78 on average) (Fig. 8b, Table S1).

5.3. Crystalline crust

The crystalline crust beneath the Borborema orogenic province (BorP in Fig. 1) and at the northwestern margin of the Paraná basin is thinner than most of the other areas (Fig. 8c). The Amazon basin has a slightly larger κ_c (mean κ_c = 1.76) than the other areas of the study region (Fig. 8d). A notable feature for the crystalline crust is that nearly all stations in the Paraná basin and Mantiqueira orogenic province [along the Brazilian coast from the southern border of the eastern São Francisco craton (16° S) to Uruguay (33°S)] have low κ_c (circled as red dashes in Fig. 8d). Especially, the κ_c in the centre of the Paraná basins (≤1.67) is much lower than normal (1.73) and other areas. The southern São Francisco basin also has a relatively low κ_c (1.71). The stations NBPN and SMTB have low κ_c but with large uncertainties (Fig. 8d) possibly because of their low-quality RFs (Figs S3a and S4c).

5.4. Whole crust

For comparison with previous studies, the total crustal thickness H_a and the average crustal κ_a are derived from the layered structures via Eq. (4). The crust beneath the northwestern edge of the Paraná basin is very thin (H_a = 31–37 km) (Table S1), the Paraná basin has average thicker crust (mean H_a = 42.7 km, Fig. 10a and Table S1) than the other basins, such as the Parnaíba basin (38.2 km), the São Francisco basin (39.6 km) and the Amazon basin (41.4 km). The thickest crust is found beneath TRCB station in the centre of the Paraná basin.

6. DISCUSSION

6.1. Method limitations

Whether the method is valid is determined by the clarity of the RF phases (Ps, M1 and M2) for the objective layer. The model with the stacking of the three phases with a highest weight for Ps (eq. 3) is the solution, so the Ps phase must be clear, and M1 and M2 are recognizable. The P-to-S phase for the Moho ($\mathrm{Ps_m}$) beneath the station TBTG (Fig. S4) may be interfered by reverberation of the sediments, so that the result on the crystalline crust contains unknown error and is not analysed here.

How fine of a layered structure is resolvable is related to the wavelength or frequency content of the RF phases: the shorter the wavelength, or the higher the frequency, the finer the resolvable structure is. Both sedimentary phases and noises can be suppressed in low-frequency receiver functions. The method here can be used in high- or low-frequency receiver functions. The uncertainty in results given here is from the landscape of the H–κ model space and the uncertainty in the given Vp (Section 4.4). However, the model space may have crowded near-parallel stripes which can cause confusions and difficulties in the solution identification. The stripes also imply that the receiver functions have unexpected or unknown peaks/troughs which can interfere the interested phases and introduce errors in the results.

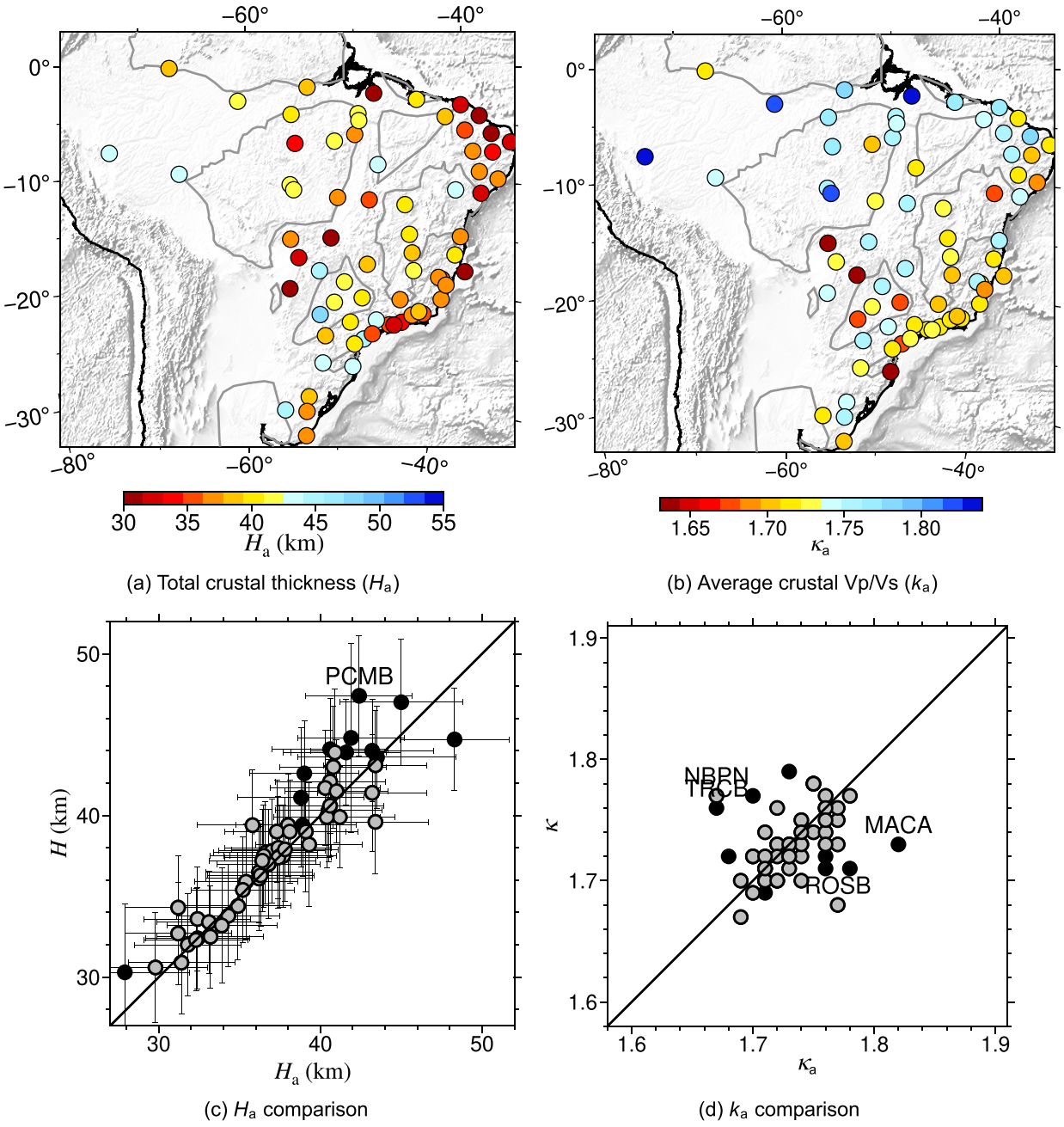

Figure 10. Total crustal thicknesses H_a (a), κ_a (b) and their comparison with H (c) and κ (d) from the standard H-κ analysis by Rivadeneyra-Vera *et al.* (2019) (RV2019). Grey-filled and black-filled circles in (c, d) are the results for stations with thin ($H_s \leq 0.3$ km) and thick sediments ($H_s > 0.3$ km), respectively. Uncertainties of H in (c) are estimated from the uncertainties in RV2019 and that caused by uncertainties of *a priori Vp* via eq. (8). The text-labelled stations in (c) are those with a large thickness difference between H and H_a (>3.5 km); in (d) are those with a large κ difference (>0.9) or large κ_a (>1.80).

6.2. Geological significance of the results on sediments

Sedimentary structure here is extracted from seismic waves at a frequency of ∼2.4 Hz converted at a seismic prominent discontinuity. The discontinuity may correspond to specific variation of geological series, but an interface of geological series is not necessarily correspondent to seismic discontinuity. Comparing our results with other measurements permits a better understanding of the seismic discontinuity.

The São Francisco basin in the São Francisco Craton (Fig. 1) is a Proterozoic intracratonic basin covered by several kilometres of Precambrian sediments and <800 m of Phanerozoic sediments (Reis *et al.* 2017). But our results did not find thick sediments in the basin (Fig. 9c), implying that the Precambrian sediments may have similar seismic properties to the underlain crystalline crust.

The sedimentary structure beneath the CSZB station in the Acre basin is well measured and permits a detailed discussion. The basin

is covered by Cenozoic erathem (Fig. 1) which often includes (e.g. Quaternary) unconsolidated sediments. The unconsolidated sediments (sands and clays) close to the CSZB is >0.15 km thick based on well-log data of CANELA FINA (Serviço Geológico do Brasil, https://siagasweb.sgb.gov.br). However, the converted phase for the topmost unconsolidated sediments is not visible in the RFs (Fig. 3a), so H–κ analysis for a two-layer model is processed (Fig. 7b). The base of the resulted sedimentary layer is at 4.1 km (Fig. 7b and Table S1), similar to the base of the Phanerozoic erathem at the depth of 4.2 km (Oliveira & Vidotti 2023). The resulted depth of sedimentary base may vary and point to a different geological interface by using different Vp, but P-wave traveltime through the sediment layer (τ_c, Table S1) is always ~1 s, consistent with the vertical two-way traveltime of 2.1 s for the P-wave previously observed in seismic reflection exploration close to the CZSB (Oliveira & Vidotti 2024). Besides, most of our derived sediment thicknesses (orange colour columns) in the Paraná basin (Fig. 9b) are generally consistent with previous studies (blue dashes).

Before strong mafic magmatism occurred in Triassic–Jurassic or Cretaceous (Almeida 1980; Zalán *et al.* 1991; Milani 1992; Milani & Filho 2000; Wanderley-Filho *et al.* 2009), the Amazon, Parnaíba and Paraná basins had been covered by thick sediments. For example, the Paraná basin is covered by six super sequences formed from Late Ordovician to Cretaceous (450–65 Ma, Almeida 1980; Zalán *et al.* 1991; Milani 1992; Milani & Filho 2000), most of which were formed before the huge basaltic lavas of the Early Cretaceous Serra Geral Formation (up to 2 km thick, LIP in Fig. 1, Milani & Filho 2000). If the magmatism strongly influenced the sediments, metamorphism (e.g. recrystallization) due to thermal effects related to the magmas may occur. Then, the sediments may become more similar to crystalline rocks in physical properties and the sediment base measured here would be no deeper than the base of the basaltic lava. However, correlation between the delay time of sediments (Ps_b) in our RF stacks (orange arrows, Figs 9a and b) and the previously determined Phanerozoic sediment bases (blue dashes, Fig. 9a,b) can be observed from station to station, especially beneath the Paraná basins, that is the greater the Ps_b, the deeper the basement (Fig. 9b). Such correlation implies that our derived sedimentary structures mainly reflect the Phanerozoic sediments of the basins and no strong metamorphism occurred in the sediments during the Triassic–Jurassic and Cretaceous magmatic events.

6.3. Comparison with previous crust thicknesses

Of the 71 stations processed in our study (Table S1), the crustal thickness and Vp/Vs for 58 stations have been previously analyzed using a standard H–κ stacking method with an assumption of single-layer model (Rivadeneyra-Vera *et al.* 2019) (RV2019). Figs 10(c) and (d) show a comparison of our H_a and κ_a with those of RV2019 (H and κ). It should be noted that the uncertainties in Fig. 10(c) are larger than in RV2019 because extra uncertainties caused by *a priori Vp* are considered here.

The difference in thickness is generally less than ~1 to 2 km (Fig. 10c). However, κ of several stations strongly deviate from the diagonal (Fig. 10d), especially for stations in areas with thick sediments (H_s > 0.3 km, black circles in Fig. 10d). We carefully checked the data and results for these stations. Most of the stations are on thick sediments (e.g. MACA station). The multiples of sediments strongly interfere with the objective stripe w_1Ps_m of the Moho and cause large uncertainty in H. The NBPN and ROSB stations with large κ deviations are not locating in sedimentary basins (Fig. 10d). The results of NBPN have large uncertainty because the Moho multiples are not clear as show in Fig. S3. In total, except for the above stations, our results are consistent with RV2019.

6.4. *Vp*/*Vs* implications

As the thicknesses of sediments and crust are generally consistent with previous measurements, we mainly focus on implication of geological information from the Vp/Vs (κ).

6.4.1. *High κ_s and κ_c in the Amazon basin*

Fig. 8(b) shows that the κ_s for all the three stations in the huge tropical rainforest area in the Amazon basin are very high (mean $\kappa_s = 2.62$), even though the stations are sparsely distributed in different sub-basins (Amazonas or Solimões basins). κ is an effective indicator not only of lithology but also of porosity for sediments (e.g. Tatham 1982; Assefa *et al.* 2003). Poisson's ratio (or κ) of water-saturated sandstones is larger than dry or weakly consolidated sandstones (Mavko *et al.* 1998). The increase of saturation (S) can cause increase of the Poisson's ratio of silty-fine sand when S is >15 per cent. Water-saturated unconsolidated sands may have a κ larger than 2.0 (Gardner & Harris 1968) due to high fluid content (Hauksson 2000; Barton 2006). So, the large κ_s observed in the Amazon basin (2.62) can hardly be interpreted only by lithology. As the Amazon basin locates within the largest tropical rainforest in the world, it is quite possible that the sedimentary rocks are highly porous and fully water saturated (S is close to 100 per cent). At least, the high κ_s indicates that the Amazon basin may be weakly consolidated or have high porosity in the sediments.

The κ_c of MACA (1.78) and MALB (1.75) are higher than the average result for Brazil (Fig. 8d). The two stations are close to an expressive long E–W gravity anomaly which have been interpreted as due to a mafic lower crust (Nunn & Aires 1988). So, the high κ_c observed in the Amazon basin are probably contributed by the existence of mafic rocks with usually high Vp/Vs ratios (e.g. Christensen 1996).

6.4.2. *Low κ_c beneath the Paraná–Etendeka LIP*

The Paraná basin and the coastal region to the east are covered by huge flood basalt (Almeida 1980; Zalán *et al.* 1991; Milani 1992; Milani & Filho 2000, the area of LIP, Fig. 8d), implying that the mafic magma related to the Tristan-Gough mantle plume (Fig. 11) may underplate or intrude and then crystallize within the crust (e.g. Ridley & Richards 2010), even though some geophysical measurements (An & Assumpção 2004b; Chaves *et al.* 2016; Dragone *et al.* 2017; Bernardes *et al.* 2023) did not observe widely mafic underplating in the Paraná basin. Vp/Vs of felsic and normal rocks increases with decreasing silica content (Kern 1982; Christensen 1996), or say, addition of mafic (low-silica content) minerals in the crust will increase κ_c. So, κ_c is a good indicator of crustal composition. The average κ_c in and around the Paraná basin where is overlapped with the Paraná–Etendeka LIP (Fig. 8d) is about 1.67 (Table S1), significantly lower than usual (1.73) and lower than other areas, implying that underplating or intrusive mafic minerals do not widely exist in the crust or the widely magmatic underplating or intruding did not happen at all. In another word, huge mantle magmas passed though

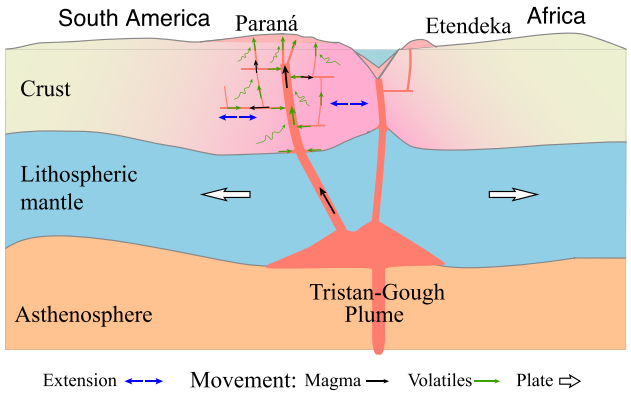

Figure 11. Carton showing magma extrusion/intrusion in the Paraná basin during the South America–Africa breaking. The crust covered by flood basalt in the Paraná basin (Almeida 1980; Zalán *et al.* 1991; Milani 1992; Milani & Filho 2000) has a lower *Vp*/*Vs*, which indicates that mantle magmas passed through but seldom underplated and intruded in the crust. In the meanwhile, the crust became hot and soft so that fluids with volatiles in the crust may be easily released (e.g. Aarnes *et al.* 2011; Ernst & Youbi 2017; Heimdal *et al.* 2020) through the vents of the ascending magmas.

the crust and formed the Paraná–Etendeka LIP but did not crystallize within the crust. The mantle magmas with low viscosity could be so buoyant due to high temperature or low-density composition as to pass though the crust so quickly that wide crystallization did not occur within the crust (Fig. 11).

Comparison of κ_c of the Paraná basin with those in the other basins (Fig. 8d) poses another interesting question. The crystalline crust beneath the Paraná-Etendeka LIP has not higher but lower κ_c than other areas. Was the crystalline crust with lower κ_c beneath the LIP resulted before, during, or after the Cretaceous magmatic event?

If it is the former case, the LIP area may have a higher silica content or more felsic minerals in the crust before the magmatic event, and then the area should have a special evolution history before and during the West Gondwana amalgamation.

If it is the latter case, the original crystalline crust had a normal *Vp*/*Vs*, but some processes with the Cretaceous magmatic event modified the crust. The mantle magma has a complex interaction with the crust (e.g. Valentine & Gregg 2008), at least will heat the crust and even lead to metamorphism or melting. The deep crust also has volatiles (Rye *et al.* 1976; Yang *et al.* 2008; Ague 2014) which are trapped in grain boundaries or combined in hydrous minerals. Metamorphic heating can release the volatiles in minerals (e.g. combined water in hydrous minerals, Shaw 1956; Fyfe *et al.* 1978; Ague 2014). Fluids with the volatiles (e.g. H_2O, CO_2) in the crust are one primary agent of chemical mass and heat transport in the deep crust (Rye *et al.* 1976; Ague 2014). The heated crust should become hot and soft so that fluids with volatiles in the crust may be easily released through the vents of the ascending magmas (illustrated in Fig. 11). A significant amount of volatiles will be released with the magmatic eruption/extrusion in a LIP (e.g. Aarnes *et al.* 2011; Ernst & Youbi 2017; Heimdal *et al.* 2020), which may cause a decrease of *Vp*/*Vs*.

The Paraná basin has *Vs* of 4.6–4.7 km s^{-1} at topmost mantle (at the 50 km, An & Assumpção 2006) which corresponds to a condition with a temperature of 690−900 °C in cratonic region using *Vs*-to-temperature conversion in An & Shi (2007), so another possibility is that the present lower crust may have a temperature close to 573 °C while Quartz, one of main crustal minerals, reaches the lowest *Vp*/*Vs* (1.27) at the temperature (Ohno 1995; Lakshtanov *et al.* 2007).

7. CONCLUSION

We retrieved the sedimentary and crystalline-crust structure for all stations of the Brazilian Seismographic Network and six new temporary stations in Brazil and Uruguay by analysing the recorded receiver functions with the *H*–κ stacking method with the aid of auxiliary stripes in the stacking image. The most interesting feature is that the Paraná–Etendeka Large Igneous Province (Paraná–Etendeka LIP) in South America, especially the Paraná basin, has a significantly lower *Vp*/*Vs* in the crystalline crust than usual and other areas, which implies that more felsic minerals exist in the present crust. This feature at least indicates that significant mafic underplating or intrusion did not happen in the crust when huge mantle magmas passed through the crust at ∼138–129 Ma. The more felsic crust beneath the Paraná–Etendeka LIP may be formed in a special evolution early than the Cretaceous magmatic event, or during the magmatic event by releasing crustal volatiles when mantle magma passed through the crust and formed the large igneous province. The resulted sedimentary thickness and *Vp*/*Vs* ratios exhibit a good correlation with the Phanerozoic sediments in the South American basins, which implies that Triassic–Jurassic and Cretaceous magmatism did not cause significant metamorphism in sediments formed before the magmatic events.

ACKNOWLEDGMENTS

This work was supported by the Natural Science Foundation of China (grants 41974051 & 42174068), the Deep Geological Survey Project of the China Geological Survey (DD20230008, DD20221643, DD20190010), Basic Research Foundation of Chinese Academy of Geological Sciences (JKY202217) and FAPESP thematic project 2013/24215–6. We thank Walid Ben-Mansour and an anonymous reviewer for the detailed and constructive comments and suggestions.

AUTHOR CONTRIBUTIONS

Meijian An (Methodology, Software, Visualization, Writing – original draft, Writing – review & editing); Mei Feng (Formal analysis, Methodology, Software, Visualization, Writing – original draft); Marcelo S. Assumpção (Writing – review & editing); Marcelo B. Bianchi (Data curation); George S. França (Data curation); Marcelo P. Rocha (Data curation) and Leda Sánchez Bettucci (Data curation, Writing – review & editing).

SUPPORTING INFORMATION

Supplementary data are available at *GJIRAS* online.

Supplementary Information

Figure S1. Receiver functions for synthetic models. The models C1, Sa and Sb are shown in Fig. 5(a); C2a and C2b in Fig. 6(a); C3 in Fig. S2a. Given a synthetic model, we generated seismograms for ray parameters (p) ranging from 0.04 to 0.076 s km^{-1} with a step of 0.005 s km^{-1} using the Raysum program (Frederiksen & Bostock 2000). Then iterative time-domain deconvolution of radial to vertical component synthetic seismograms (Ligorría & Ammon 1999) by using Gaussian pulse factor 5 was processed to extract

receiver functions with a centre frequency of ∼2.4 Hz, same as those applied to real observations. The receiver functions of Sa contain strong phases of reflections and conversions.

Figure S2. *H–κ* analysis for a three-layer crust model. (a) Synthetic input model. (b) Full model space for the model C3. (c) Zoomed-in model space for the sediment layers. Model C3 is covered with an extra thin unconsolidated sedimentary layer over the model C2b (Fig. 6a). *Vp* of 6.1 km s^{-1} used for calculations in (b, c) is strongly different from *Vp* in layers 1 and 2, so the resulted thicknesses and *Vp*/*Vs* for the two layers in the model space in (b, c) have observable deviation from the true model in (a). The symbols are the same as in Fig. 6. The star on stripe w_1Ps_m in (b) marks the average crustal solution of the three-layered model (H_a, κ_a) obtained by eq. (4); the star on stripe w_1Ps_2 in (c) marks the average sedimentary solution of the two sedimentary layers obtained by eq. (4).

Figure S3. Receiver functions of the station NBPN (a) and the model space of the *H*—*κ* analysis (b). The Moho multiples in (a) and the stacking stripes for multiples in (b) are not clear.

Figure S4. Receiver functions (a, c) and *H–κ* model spaces (b, d) for the station TBTG and SMTB. Ps_m of the two stations are mixed with sedimentary resonances.

Figure S5. Receiver functions of NBIT station. The receiver functions for ray parameters (p) of >0.07 have two remarkable phases at ∼4.6 and 6.8 s. If the latter is Ps_m, the crustal thickness will be much thicker than nearby stations, so we chose using the former as Ps_m.

Table S1. Results of sediment and crystalline crust

Please note: Oxford University Press is not responsible for the content or functionality of any supporting materials supplied by the authors. Any queries (other than missing material) should be directed to the corresponding author for the paper.

DATA AVAILABILITY

New observation from portable seismic stations is restricted but available on reasonable request; the other seismic data are available at http://rsbr.on.br/(Bianchi *et al.* 2018). All figures are made with Generic Mapping Tools (Wessel *et al.* 2013). Receiver functions from raw seismic waveforms are retrieved via codes in Computer Programs in Seismology (Herrmann 2013). Synthetic seismograms are made with the Raysum program (Frederiksen & Bostock 2000).

REFERENCES

Aarnes, I., Fristad, K., Planke, S. & Svensen, H., 2011. The impact of host-rock composition on devolatilization of sedimentary rocks during contact metamorphism around mafic sheet intrusions, *Geochem. Geophys. Geosyst.,* **12**(10), doi:10.1029/2011GC003636.

Ague, J.J., 2014. 4.6–Fluid flow in the deep crust, in *Treatise on Geochemistry,* 2nd edn, pp. 203–247, eds, Holland, H. D. & Turekian, K. K., Elsevier.

Akinremi, S., van der Meijde, M., Thomas, C., Afonso, J.C., Ruigrok, E. & Fadel, I., 2024. Waveform fitting of receiver functions for enhanced retrieval of crustal structure in the presence of sediments, *J. geophys. Res.,* **129**(5), e2023JB028393.

Almeida, F.F.M., 1980. *Tectonica Da Bacia do Parana no Brasil,* PAULIPETRO.

Ammon, C.J., 1991. The isolation of receiver effects from teleseismic P waveforms, *Bull. seism. Soc. Am.,* **81,** 2504–2510.

An, M. & Assumpção, M., 2004a. Basement depth in the Parana´ basin with high frequency receiver functions (extended abstract), in *1st Regional Symposium of Brazilian Geophysical Society,* September 2004, São Paulo, Brazil, cp-216-00030, European Association of Geoscientists & Engineers.

An, M. & Assumpção, M.S., 2004b. Multi-objective inversion of surface waves and receiver functions by competent genetic algorithm applied to the crustal structure of the Paraná Basin, SE Brazil, *Geophys. Res. Lett.,* **31**(5), doi:10.1029/2003GL019179.

An, M. & Assumpção, M.S., 2006. Crustal and upper mantle structure in intracratonic Paraná Basin, SE Brazil, from surface wave dispersion using genetic algorithm, *J. S. Am. Earth Sci.,* **21**(3), 173–184.

An, M. & Shi, Y., 2007. 3D crustal and upper-mantle temperature of the Chinese continent, *Sci. China Ser. D-Earth Sci.,* **50**(10), 1441–1451.

Assefa, S., McCann, C. & Sothcott, J., 2003. Velocities of compressional and shear waves in limestones, *Geophys. Prospect.,* **51**(1), 1–13.

Assumpção, M., Feng, M., Tassara, A. & Julià, J., 2013. Models of crustal thickness for South America from seismic refraction, receiver functions and surface wave tomography, *Tectonophysics,* **609,** 82–96.

Barton, N., 2006. *Rock Quality, Seismic Velocity, Attenuation and Anisotropy,* 1st edn, 729, CRC Press.

Bauer, S.J. & Conley, C.H., 1987. A proposed method for predicting rock-mass deformability using a compliant joint model, in *Paper presented at the The 28th U.S. Symposium on Rock Mechanics (USRMS),* Tucson, Arizona, 29 June–1 July, 1987.

Bernardes, R.B., Soares, J.E.P., Lima, M.V.A.G.d., Fuck, R.A. & Viana, A.R., 2023. Cretaceous magmatic underplating and delamination beneath continental SE Brazil and their tectonic implications: evidence from the PABBRISE wide-angle reflection and refraction seismic profile, *Tectonophysics,* **856,** 229856, doi:10.1016/j.tecto.2023.229856.

Bhasin, R. & Høeg, K., 1998. Numerical modelling of block size effects and influence of joint properties in multiply jointed rock, *Tunnell. Undergr. Space Technol.,* **13**(2), 181–188.

Bianchi, M.B. *et al.*, 2018. The Brazilian seismographic Network (RSBR): improving seismic monitoring in Brazil, *Seismol. Res. Lett.,* **89**(2A), 452–457.

Cedraz, V., Julià, J. & Assumpção, M., 2020. Joint inversion of receiver functions and surface-wave dispersion in the Pantanal wetlands: implications for basin formation, *J. geophys. Res.,* **125**(2), e2019JB018337.

Chaput, J. *et al.*, 2014. The crustal thickness of West Antarctica, *J. geophys. Res.,* **119**(1), 378–395.

Chaves, C., Ussami, N. & Ritsema, J., 2016. Density and P-wave velocity structure beneath the Paraná Magmatic Province: refertilization of an ancient lithospheric mantle, *Geochem. Geophys. Geosyst.,* **17**(8), 3054–3074.

Cho, T., 2011. Removing reverberation in ice sheets from receiver functions, *Seismol. Res. Lett.,* **82**(2), 207–210.

Christensen, N.I., 1996. Poisson's ratio and crustal seismology, *J. geophys. Res.,* **101**(B2), 3139–3156.

Clitheroe, G., Gudmundsson, O. & Kennett, B.L.N., 2000. Sedimentary and upper crustal structure of Australia from receiver functions, *Aust. J. Earth Sci.,* **47**(2), 209–216.

Coffin, M.F., Gahagan, L.M., Lawver, L.A. & Dalziel, I.W.D., 2013. *Large Igneous Provinces: Map and Data,* Institute for Geophysics, University of Texas.

Cordani, U.G., Ramos, V.A., Fraga, L.M., Cegarra, M., Delgado, I., de Souza, K.G., Gomes, F.E.M. & Schobbenhaus, C. 2016. *Explanatory Notes: Tectonic Map of South America,* 2nd edn, scale 1:5 000 000, 13 pp, Paris.

Crotwell, H.P. & Owens, T.J., 2005. Automated receiver function processing, *Seismol. Res. Lett.,* **76**(6), 702–709.

Dahl-Jensen, T. *et al.*, 2003. Depth to Moho in Greenland: receiver-function analysis suggests two proterozoic blocks in Greenland, *Earth planet. Sci. Lett.,* **205**(3), 379–393.

Dragone, G.N., Ussami, N., Gimenez, M.E., Lince Klinger, F.G. & Chaves, C.A.M., 2017. Western Paraná suture/shear zone and the limits of Rio Apa, Rio Tebicuary and Rio de la Plata cratons from gravity data, *Precambrian Res.,* **291,** 162–177.

Dunn, M.L. & Ledbetter, H., 1995. Poisson's ratio of porous and microcracked solids: theory and application to oxide superconductors, *J. Mater. Res.,* **10**(11), 2715–2722.

Eaton, D.W., Dineva, S. & Mereu, R., 2006. Crustal thickness and VP/VS variations in the Grenville orogen (Ontario, Canada) from analysis of teleseismic receiver functions, *Tectonophysics,* **420**(1), 223–238.

Efron, B. & Tibshirani, R., 1991. Statistical data analysis in the computer age, *Science,* **23**(5018), 390–395.

Ernst, R.E. & Youbi, N., 2017. How large igneous provinces affect global climate, sometimes cause mass extinctions, and represent natural markers in the geological record, *Palaeogeogr. Palaeoclimatol. Palaeoecol.,* **478,** 30–52.

Feng, M. *et al.*, 2014. Structure of the crust and mantle down to 700 km depth beneath the East Qaidam basin and Qilian Shan from *P* and *S* receiver functions, *Geophys. J. Int.,* **199**(3), 1416–1429.

Feng, M., An, M. & Dong, S., 2017. Tectonic history of the Ordos Block and Qinling Orogen inferred from crustal thickness, *Geophys. J. Int.,* **210**(1), 303–320.

Frederiksen, A.W. & Bostock, M.G., 2000. Modelling teleseismic waves in dipping anisotropic structures, *Geophys. J. Int.,* **141**(2), 401–412.

Fyfe, W.S., Price, N.J. & Thompson, A.B., 1978. *Fluids in the Earth's Crust: Their Significance in Metamorphic, Tectonic and Chemical Transport Process,* Elsevier, 401.

Gao, X., Li, Y., Yang, X. & Ren, Z., 2022. Crustal structure beneath the central and western North China from receiver function analysis, *Earthq. Sci.,* **35**(6), 448–473.

Gardner, G.H.F. & Harris, M.H., 1968. Velocity and attenuation of elastic waves In sands, in *Presented at SPWLA 9th Annual Logging Symposium,* New Orleans, Louisiana, 23–26 June 1968.

Gercek, H., 2007. Poisson's ratio values for rocks, *Int. J. Rock Mech. Min. Sci.,* **44**(1), 1–13.

Góes, A.M.O. & Feijó, F.J., 1994. Bacia do Parnaíba, *Boletim de Geociências da Petrobrás,* **8,** 57–67.

Hajra, S., Hazarika, D., Bankhwal, M., Kundu, A. & Kumar, N., 2019. Average crustal thickness and Poisson's ratio beneath the Kali River Valley, Kumaon Himalaya, *J. Asian Earth Sci.,* **173,** 176–188.

Hauksson, E., 2000. Crustal structure and seismicity distribution adjacent to the Pacific and North America plate boundary in southern California, *J. geophys. Res.,* **105**(B6), 13 875–13 903.

Heimdal, T.H., Jones, M.T. & Svensen, H.H., 2020. Thermogenic carbon release from the Central Atlantic magmatic province caused major end-triassic carbon cycle perturbations, *Proc. Natl. Acad. Sci.,* **117**(22), 11 968–11 974.

Herrmann, R.B., 2013. Computer Programs in seismology: an evolving tool for instruction and research, *Seismol. Res. Lett.,* **84**(6), 1081–1088.

Julià, J., Ammon, C.J., Herrmann, R.B. & Correig, A.M., 2000. Joint inversion of receiver function and surface wave dispersion observations, *Geophys. J. Int.,* **143,** 99–112.

Kern, H., 1982. Elastic-wave velocity in crustal and mantle rocks at high pressure and temperature: the role of the high-low quartz transition and of dehydration reactions, *Phys. Earth planet. Inter.,* **29**(1), 12–23.

Lakshtanov, D.L., Sinogeikin, S.V. & Bass, J.D., 2007. High-temperature phase transitions and elasticity of silica polymorphs, *Phys. Chem. Miner.,* **34**(1), 11–22.

Langston, C.A., 1979. Structure under Mount Rainier, Washington, inferred from teleseismic body waves, *J. geophys. Res.,* **84**(B9), 4749–4762.

Langston, C.A., 2011. Wave-field continuation and decomposition for passive seismic imaging under deep unconsolidated sediments, *Bull. seism. Soc. Am.,* **101**(5), 2176–2190.

Lawrence, J.F., Wiens, D.A., Nyblade, A.A., Anandakrishnan, S., Shore, P.J. & Voigt, D., 2006. Crust and upper mantle structure of the Transantarctic Mountains and surrounding regions from receiver functions, surface waves, and gravity: implications for uplift models, *Geochem. Geophys. Geosyst.,* **7**(10), doi:10.1029/2006GC001282.

Leahy, G.M., Saltzer, R.L. & Schmedes, J., 2012. Imaging the shallow crust with teleseismic receiver functions, *Geophys. J. Int.,* **191**(2), 627–636.

Ligorría, J.P. & Ammon, C.J., 1999. Iterative deconvolution and receiver-function estimation, *Bull. seism. Soc. Am.,* **89,** 1395–1400.

Martinod, J., Husson, L., Roperch, P., Guillaume, B. & Espurt, N., 2010. Horizontal subduction zones, convergence velocity and the building of the Andes, *Earth planet. Sci. Lett.,* **299**(3), 299–309.

Mavko, G., Mukerji, T. & Dvorkin, J., 1998. *The Rock Physics Handbook,* Cambridge Univ. Press, 329.

Milani, E.J. & Filho, A.T., 2000. Sedimentary basins of South America, in *Tectonic Evolution of South America, 31st International Geological Congress,* 389–449, eds Cordani, U. G., Milani, E. J., Filho, A. T. & Campos, D. A., SciELO.

Milani, E.J.D., 1992. *Intraplate Tectonics and the Evolution of the Paraná Basin, SE Brazil, Presented at Inversion Tectonics of the Cape Fold Belt,* Karoo and Cretaceous basins of Southern Africa.

Min, K.-B. & Jing, L., 2003. Numerical determination of the equivalent elastic compliance tensor for fractured rock masses using the distinct element method, *Int. J. Rock Mech. Min. Sci.,* **40**(6), 795–816.

Mooney, W.D., Laske, G. & Masters, G., 1998. CRUST5.1: a global crustal model at 5° × 5°, *J. geophys. Res.,* **103**(B1), 727–747.

Nascimento, A.V.d.S., França, G.S., Chaves, C.A.M. & Marotta, G.S.A., 2021. Rayleigh wave group velocity maps at periods of 10–150 s beneath South America, *Geophys. J. Int.,* **228**(2), 958–981.

Nunn, J.A. & Aires, J.R., 1988. Gravity anomalies and flexure of the lithosphere at the Middle Amazon basin, Brazil, *J. geophys. Res.,* **93**(B1), 415–428.

Ogden, C.S., Bastow, I.D., Gilligan, A. & Rondenay, S., 2019. A reappraisal of the H–κ stacking technique: implications for global crustal structure, *Geophys. J. Int.,* **219**(3), 1491–1513.

Ohno, I., 1995. Temperature variation of elastic properties of α- quartz up to the α-β transition, *J. Phys. Earth,* **43**(2), 157–169.

Oliveira, R.S. d. & Vidotti, R.M., 2023. The Acre Basin basement (NW Brazil) and the transition from the intracratonic to retroarc foreland basin system, *Basin. Res.,* **35**(1), 86–119.

Oliveira, R.S.d. & Vidotti, R.M., 2024. The role of tectonic inheritance in the development of an Andean retroarc foreland basin system: the Acre Basin (NW Brazil), *Mar. Petrol. Geol.,* **160,** doi:10.1016/j.marpetgeo.2023.106645.

Owens, T.J., Zandt, G. & Taylor, S.R., 1984. Seismic evidence for an ancient rift beneath the Cumberland Plateau, Tennessee: a detailed analysis of broadband teleseismic P waveforms, *J. Geophys. Res.,* **89,** 7783–7795.

Reis, H.L.S., Alkmim, F.F., Fonseca, R.C.S., Nascimento, T.C., Suss, J.F. & Prevatti, L.D., 2017. The São Francisco Basin, in *São Francisco Craton, Eastern Brazil: Tectonic Genealogy of a Miniature Continent,* 117–143, eds, Heilbron, M. , *et al.*, Springer International Publishing.

Ridley, V.A. & Richards, M.A., 2010. Deep crustal structure beneath large igneous provinces and the petrologic evolution of flood basalts, *Geochem. Geophys. Geosyst.,* **11**(9), doi:10.1029/2009GC002935.

Rivadeneyra-Vera, C., 2019. An updated crustal thickness map of Central South America based on receiver function measurements in the region of the Chaco, Pantanal, and Paraná Basins, southwestern Brazil, *J. geophys. Res.,* **124**(8), 8491–8505.

Rye, R.O., Schuiling, R.D., Rye, D.M. & Jansen, J.B.H., 1976. Carbon, hydrogen, and oxygen isotope studies of the regional metamorphic complex at Naxos, Greece, *Geochim. Cosmochim. Acta,* **40**(9), 1031–1049.

Schenk, C.J., Viger, R.J. & Anderson, C.P., 1999. Maps Showing Geology, Oil and Gas Fields and Geologic Provinces of the South America Region. Report, Reston, VA.

Sensarma, S., Storey, B.C. & Malviya, V.P., 2018. Gondwana large igneous provinces (LIPs): distribution, diversity and significance, *Geol. Soc., Lond., Spec. Publ.,* **463**(1), 1–16.

Shaw, D.M., 1956. Geochemistry of Pelitic Rocks. Part III: major elements and general Geochemistry, *GSA Bull.,* **67**(7), 919–934.

Sheehan, A.F., Abers, G.A., Jones, C.H. & Lerner-Lam, A.L., 1995. Crustal thickness variations across the Colorado Rocky Mountains from teleseismic receiver functions, *J. geophys. Res.,* **100**(B10), 20 391–20 404.

Shirzad, T., Assumpcao, M. & Bianchi, M., 2019. Ambient seismic noise tomography in west-central and Southern Brazil, characterizing the crustal

structure of the Chaco-Paraná, Pantanal and Paraná basins, *Geophys. J. Int.,* **220**(3), 2074–2085.

Tao, K. *et al.*, 2014b. Crustal structure beneath NE China imaged by NECESSArray receiver function data, *Earth planet. Sci. Lett.,* **398,** 48–57.

Tao, K., Liu, T., Ning, J. & Niu, F., 2014a. Estimating sedimentary and crustal structure using wavefield continuation: theory, techniques and applications, *Geophys. J. Int.,* **197**(1), 443–457.

Tatham, R.H., 1982. Vp/Vs and lithology, *Geophysics,* **47**(3), 336–344.

Valentine, G.A. & Gregg, T.K.P., 2008. Continental basaltic volcanoes—processes and problems, *J. Volc. Geotherm. Res.,* **177**(4), 857–873.

Wanderley-Filho, J.R., Eiras, J.F., da Cruz Cunha, P.R. & van der Ven, P.H., 2009. The paleozoic Solimões and Amazonas Basins and the Acre Foreland Basin of Brazil, in *Amazonia: Landscape and Species Evolution,*. 29–37, eds Hoorn, C. & Wesselingh, F. P., Blackwell Publishing Ltd.

Wei, Z., Chu, R., Chen, L., Wu, S., Jiang, H. & He, B., 2020. The structure of the sedimentary cover and crystalline crust in the Sichuan Basin and its tectonic implications, *Geophys. J. Int.,* **223**(3), 1879–1887.

Wei, Z., Chu, R., Wang, J., Ling, Y., Hu, J. & Wu, S., 2023. E-W and S-N differences in the sedimentary cover and crystalline crust in the cratonic Ordos Basin from receiver function analysis, *J. geophys. Res.,* **128**(2), e2022JB025696.

Wessel, P., Smith, W.H.F., Scharroo, R., Luis, J. & Wobbe, F., 2013. Generic Mapping tools: improved version released, *EOS, Trans. Am. geophys. Un.,* **94**(45), 409–410.

White, R. & McKenzie, D., 1989. Magmatism at rift zones: the generation of volcanic continental margins and flood basalts, *J. geophys. Res.,* **94**(B6), 7685–7729.

Yang, X.-Z., Deloule, E., Xia, Q.-K., Fan, Q.-C. & Feng, M., 2008. Water contrast between precambrian and phanerozoic continental lower crust in eastern China, *J. geophys. Res.,* **113**(B8), doi:10.1029/2007JB005541.

Yeck, W.L., Sheehan, A.F. & Schulte-Pelkum, V., 2013. Sequential H-κ stacking to obtain accurate crustal thicknesses beneath sedimentary basins, *Bull. seism. Soc. Am.,* **103**(3), 2142–2150.

Yu, Y., Song, J., Liu, K.H. & Gao, S.S., 2015. Determining crustal structure beneath seismic stations overlying a low-velocity sedimentary layer using receiver functions, *J. geophys. Res.,* **120**(5), 3208–3218.

Zalán, P., Wolff, S., Conceição, J.C.J., Astolfi, M.A.M., Vieira, I.S., Appi, V.T., Zanotto, O.A. & Marques, A., 1991. Tectonics and sedimentation of the Paraná Basin, in *Gondwana Seven Proceedings,* 83–117.

Zhang, Y. & Huang, J., 2019. Structure of the sediment and crust in the Northeast North China craton from improved sequential H-k stacking method, *Open Geosci.,* **11**(1), 682–696.

Zhang, Z. & Olugboji, T., 2021. The signature and elimination of sediment reverberations on submarine receiver functions, *J. geophys. Res.,* **126**(5), e2020JB021567, 10.1029/2020JB021567.

Zhang, Z. & Olugboji, T., 2023. Lithospheric imaging through reverberant layers: sediments, oceans, and glaciers, *J. geophys. Res.,* **128**(5), e2022JB026348, 10.1029/2022JB026348.

Zhu, H., Tian, Y., Liu, C. & Feng, X., 2018. Estimation of the crustal structure beneath the sedimentary Basin: predictive deconvolution method to remove multiples reverberations of the receiver function, *Chinese J. Geophys.,* **61**(9), 3664–3675.

Zhu, L. & Kanamori, H., 2000. Moho depth variation in southern California from teleseismic receiver functions, *J. geophys. Res.,* **105**(B2), 2969–2980.